Geomorphology and geological controls of an active paraglacial rockslide in the New Zealand Southern Alps

Cody, Emma ; Draebing, Daniel ; Cook, Simon; McColl, Samuel ; Brideau, Marc-Andre

Published in:
Landslides

DOI:
10.1007/s10346-019-01316-2

Publication date:
2019

Document Version
Peer reviewed version

Geomorphology and geological controls of an active paraglacial rockslide in the New Zealand Southern Alps.

Emma Cody[1], Daniel Draebing[2,3], Sam McColl[1], Simon Cook[4], Marc-Andre Brideau[5]

[1] Geosciences Group, School of Agriculture and Environment, Massey University, New Zealand

[2] Chair of Geomorphology, University of Bayreuth, Germany

[3]Chair of Landslide Research, Technical University of Munich, Germany

[4]Geography and Environmental Science, School of Social Sciences, University of Dundee, United Kingdom

[5]GNS Science, Lower Hutt, New Zealand

Acknowledgements

The research was funded by Massey University Research Grant (MR19350), Brian Mason Trust (2017/24) and Deutsche Forschungsgemeinschaft (DR 1070/1-1). The authors acknowledge support by the Department of Conservation. S. Cook and D. Draebing thank Massey University for funding in the form of the Massey University Visiting International Research Fund (2017 and 2018 respectively).

Field work was kindly supported by Jana Eichel, Pat Kailey, Tim Stahl, Michal Brezny, James Fay and Florian Strohmaier with laboratory analysis by Georg Stockinger, Fritz Ettl and Till Mayer.

Abstract

Geological structures precondition hillslope stability as well as the processes and landslide mechanisms which develop in response to deglaciation. In areas experiencing glacier retreat and debuttressing, identifying landslide preconditions is fundamental for anticipating landslide development. Herein, the ~150 M m³ Mueller Rockslide in Aoraki/Mount Cook National Park, New Zealand is described, and we document how preconditions have controlled its morphology and development in response to thinning of the adjacent Mueller Glacier. A combination of geomorphological and geotechnical mapping – based on field, geophysical and remote sensing data – was used to characterise the rock mass and morphology of the rockslide and surrounding hillslope. Mueller Rockslide is identified as a rock compound slide, undergoing dominantly translational failure on a dip slope. The crown of the rockslide is bounded by several discontinuous, stepped scarps whose orientation is controlled by joint sets; these scarps form a zone of toppling that is delivering rock debris to the main rockslide body. Surface and subsurface discontinuity mapping above the crown identified numerous joints, fractures and several scarps that may facilitate continued retrogressive enlargement of the rockslide. The presence of lateral release structures, debuttressing of the rockslide toe and steeply dipping bedding, suggest the rockslide may be capable of evolving to rapid failure.

Keywords: Paraglacial, Rockslide, Landslide Preconditions, UAV, Natural Hazard

Introduction

Topographic, environmental and geological conditions predispose alpine landscapes to hillslope instability (McColl and Draebing 2019). Consequently, mass movements are a significant process shaping alpine and mountainous areas as well as a significant natural hazard. While slope failure can occur in a variety of ways in mountainous terrain, large deep seated slope failures such as deep seated gravitational slope deformations (DSGSD) and rockslides are primary hillslope modification processes and their evolution remains a subject of scientific enquiry.

DSGSD predominantly occur in steep relief and are commonly expressed as large interconnected networks of fractures and tensions cracks as well as with toe bulging, uphill and downhill facing scarps and significantly displaced geomorphic features (Beck 1968; Dramis et al. 1994; Bovis et al. 1996; Algiardi et al. 2001; Agliardi et al. 2009a). DSGSD deform slowly over centuries to millennia (El Bedoui et al. 2009; Agliardi et al. 2009b; Pánek et al. 2011b; Pánek and Klimes 2016), however, they have the potential to accelerate and fail

68 catastrophically as large rockslides or rock avalanches (Pánek et al. 2009; Kilburn and Petley
69 2003; Gori et al. 2014). Rockslides, whether preceded or not by DSGSD activity, can reach
70 similar sizes to DSGSD (>100Mm^3) but differ in that they more commonly move via sliding
71 along one or more discrete failure surfaces, rather than through internal deformation and toe
72 bulging (Hungr et al. 2014). Upward facing scarps are less characteristic of rockslides, and they
73 tend to involve more intact rock mass blocks in comparison to DSGSD (Crosta and Agliardi
74 2003; Crosta et al. 2014). As with DSGSD, they can fail progressively, evolving towards rapid
75 failure, but may involve different failure processes.
76 Given the potentially large size (>100 Mm^3) of DSGSDs and rockslides and their ability to
77 generate long-runout, rock avalanches, these slope failures are considered to be a major natural
78 hazard in alpine landscapes. Although they have long been recognised within the scientific
79 community (Nemcok 1972; Mahr 1977; Radbruch-Hall 1978; Bovis 1982; Crosta et al. 2013;
80 Chigira and Kiho 1994), there is still much to understand of the processes driving their
81 evolution towards failure. As these large rockslope failures often develop over centuries to
82 millennia, as well as occurring in steep and difficult terrain, understanding internal factors
83 influencing development is critical for assessing the failure potential of the landslide.
84 Worldwide, many large DSGSD and rockslides have been recognised in oversteepened glacial
85 valleys (Agliardi et al. 2009b; McColl and Davies 2013; Barbarano et al. 2015; Coquin et al.
86 2015). In alpine landscapes, glacier debuttressing – where ice support is removed from the toe
87 of a hillslope – is considered a primary influence on preparing DSGSD or rockslide formation
88 (Ballantyne 2002). However, rainfall and changes in groundwater (Pánek et al. 2011a; Nishii
89 et al. 2013), earthquakes (Crozier et al. 1995; Aringoli et al. 2016), gravitational or topographic
90 stresses (Martinotti et al. 2011) and river incision (Hou et al. 2014) have all been attributed
91 with triggering hillslope failures in both glaciated and non-glaciated terrain. Given that large
92 rock slope failures occur in a variety of rock types and rock masses, climate conditions, and
93 tectonic settings, identifying a common control or main trigger is difficult. As it stands, DSGSD
94 and rockslides appear to commonly form along pre-existing or reactivated tectonic structures
95 (faults, fractures, joints) (Agliardi et al. 2001; Ghirotti et al. 2011; Ambrosi and Crosta 2011;
96 Jaboyedoff et al. 2013) which constrain their size and morphology. Geological structures and
97 steep relief precondition instabilities and are key for understanding how preparatory factors
98 like debuttressing, fluvial incision and strength degradation allow slopes to evolve to failure.
99 Investigations into DSGSD and rockslides in glaciated valleys have primarily focused on those
100 which formed or failed following prehistoric (pre Little Ice Age; LIA) glacier retreat (Cossart
101 et al. 2008; Hewitt et al. 2008; Ballantyne et al. 2013; Ballantyne et al. 2014a; Ballantyne et al.

2014b; Ballantyne and Stone 2009) as a result of debuttressing and loss of support to the slope. More recently, effort has been directed towards monitoring the response of hillslopes currently undergoing deformation following glacier retreat (Clayton et al. 2017; Fey et al. 2017; Kos et al. 2017; Glueer et al. 2019). For example, an acceleration of landslide movement and a change in movement mechanisms have been observed to coincide with glacier retreat and debuttressing at the Moosfluh Landslide aside the Aletsch Glacier in Switzerland (Kos et al. 2017; Glueer et al. 2019) and at the Marzell Rockslide in Austria (Fey et al. 2017).

While monitoring studies have highlighted how some slopes are currently accelerating in response to recent glacier retreat, deformation may have been occurring within the rock slope for centuries to millenia (Eberhardt et al. 2004; Brideau et al. 2009; Ballantyne et al. 2014a; Riva et al. 2017). Progressive failure (i.e. the progressive loss of strength of a rock mass) within paraglacial rockslopes occurs through stress changes induced by glacial erosion, ice load fluctuations, in-situ stress modification and thermal and hydro-mechanical processes (McColl 2012a; Jaboyedoff et al. 2013; Grämiger et al. 2017; Grämiger et al. 2018). While a rockslope may currently be undergoing rapid deformation, it is likely strength degradation has been ongoing through several repeated cycles of glacier advance and retreat. Further, as glaciated slopes begin to develop instability, their movement might involve deformation of its buttressing glacier (McColl and Davies 2013), creating a complex interaction between the glacier and the mass movement. Such interactions are likely to affect whether a slope catastrophically collapses, the timing of collapse, and how the mass movement affects glacier and sediment transport dynamics.

In this study, we investigate the geomorphology and structural features of an active deep seated slope failure, The Mueller Rockslide, whose development coincides with thinning of an adjacent glacier. The Mueller Rockslide was described by McColl and Davies (2013) as an example of a large (~150 Mm^3) deep-seated gravitational slope deformation, undergoing gradual deformation adjacent to a retreating glacier. The study combines geomorphological mapping with geotechnical, geophysical and remote sensing techniques to identify discontinuity sets and other structures in and around the rockslide. The structures are interpreted within the context of the geomorphological and geological setting of the rockslide. We explore how these structures have preconditioned failure of this slope and identify the potential for retrogressive enlargement and catastrophic development of the rockslide. Our research contributes to the understanding of how geological structures precondition paraglacial rock slope failures and influence their response to contemporary glacier retreat.

Study area

Mueller Rockslide is in Aoraki/ Mount Cook National Park, New Zealand (Fig. 1), situated on the western flank of the Sealy Range. The rockslide was first identified by Hancox (1994), as part of a study on the stability of an alpine mountain hut. At that time, the hut (referenced as Old Hut herein) was situated on the eastern edge of the Sealy Range, which was experiencing localised subsidence in a large slump block. Due to safety concerns, the hut was removed and rebuilt 500 m south-west along the range in 2003. During the investigation, Hancox (1994) identified and described a much large slope failure (herein the Mueller Rockslide), affecting the western side of the Sealy Range, which Hancox described as a large block slide with an extensive headscarp area and a large rift-zone / graben. The hut is now about 200 m east of a series of large (10-20 m high, 30-50 m long) scarps that appear to define the headscarp of the rockslide (Hancox 1998). Above the rockslide, in the vicinity of the newly located Mueller Hut, several large fractures have been monitored since 1994 with opening detected of between 6 and 66 mm (Archibald et al. 2016). Annual GPS measurements of survey pins about 700 m west of Mueller Hut within the rockslide indicate movement rates of 1 m per year between 2010 and 2012 (McColl 2012b).

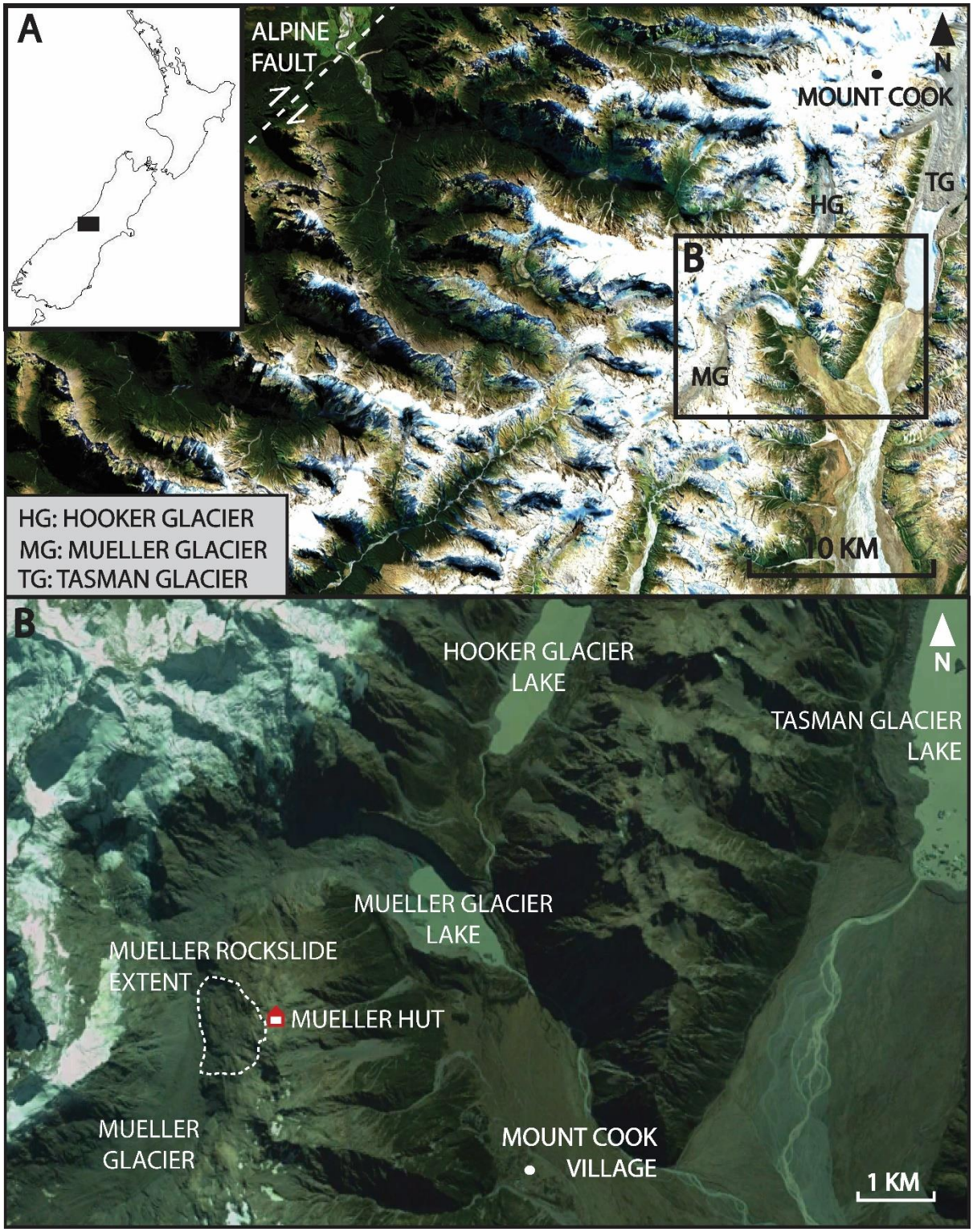

Figure 1. A) Location map of Mount Cook and surrounding area. B) Mount Cook Village and surrounding area. Mueller Rockslide estimated boundary is represented by the dashed white line with Mueller Hut sitting to the east.

The shape and stability of the Sealy Range reflects its history of tectonic and glacial processes. The range is about 25 km east of the boundary between the Pacific and Australian tectonic plates, which for the past 5 million years has been expressed by the Alpine Fault. Regional

shortening and compression has resulted in faulting, folding and fracturing of the Torlesse Group greywacke sandstones and argillite, and semischist (low-grade schist of textural zone IA, IIB) which make up the Sealy Range (Cox and Barrell 2007). The Mueller Rockslide is located on the western side of the Sealy Range, on the western limb of the tightly folded north-plunging Kitchener anticline (Lillie and Gunn 1964), which formed initially from east-west compression (Fig. 2). Within and near the rockslide body, bedding dips westward at roughly 30-60 degrees, with the Mueller Rockslide forming within the dip slope of the interbedded greywacke (Lillie and Gunn 1964; McColl and Davies 2013) although most of this is heavily mantled with debris material. Currently, the Mueller Rockslide abuts onto the margin of the Mueller Glacier, which is undergoing rapid thinning and terminus retreat. The Mueller Glacier has retreated by over 1 km (Gellatly 1985; Kirkbride and Warren 1999) since the Little Ice Age (LIA) ~200-250 years ago (Fig. 1), but it is still approximately 3.5 km down-valley from the Mueller Rockslide (Winkler 2018). Glacier debuttressing has occurred through thinning of the glacier and has been in the order of some 100 metres since the LIA, as inferred here from abandoned lateral moraine ridges on the slopes near the rockslide as well as documented at the terminus (Gellatly 1985; Kirkbride and Warren 1999). The remaining thickness of the glacier at the toe of the Mueller Rockslide is unknown, but based on valley cross-section extrapolation, is estimated to be < 100 metres thick at the southern (upper valley) end of the rockslide. The glacier at the northern end may have melted completely, becoming disconnected from the down valley end of the glacier (Fig. 2).

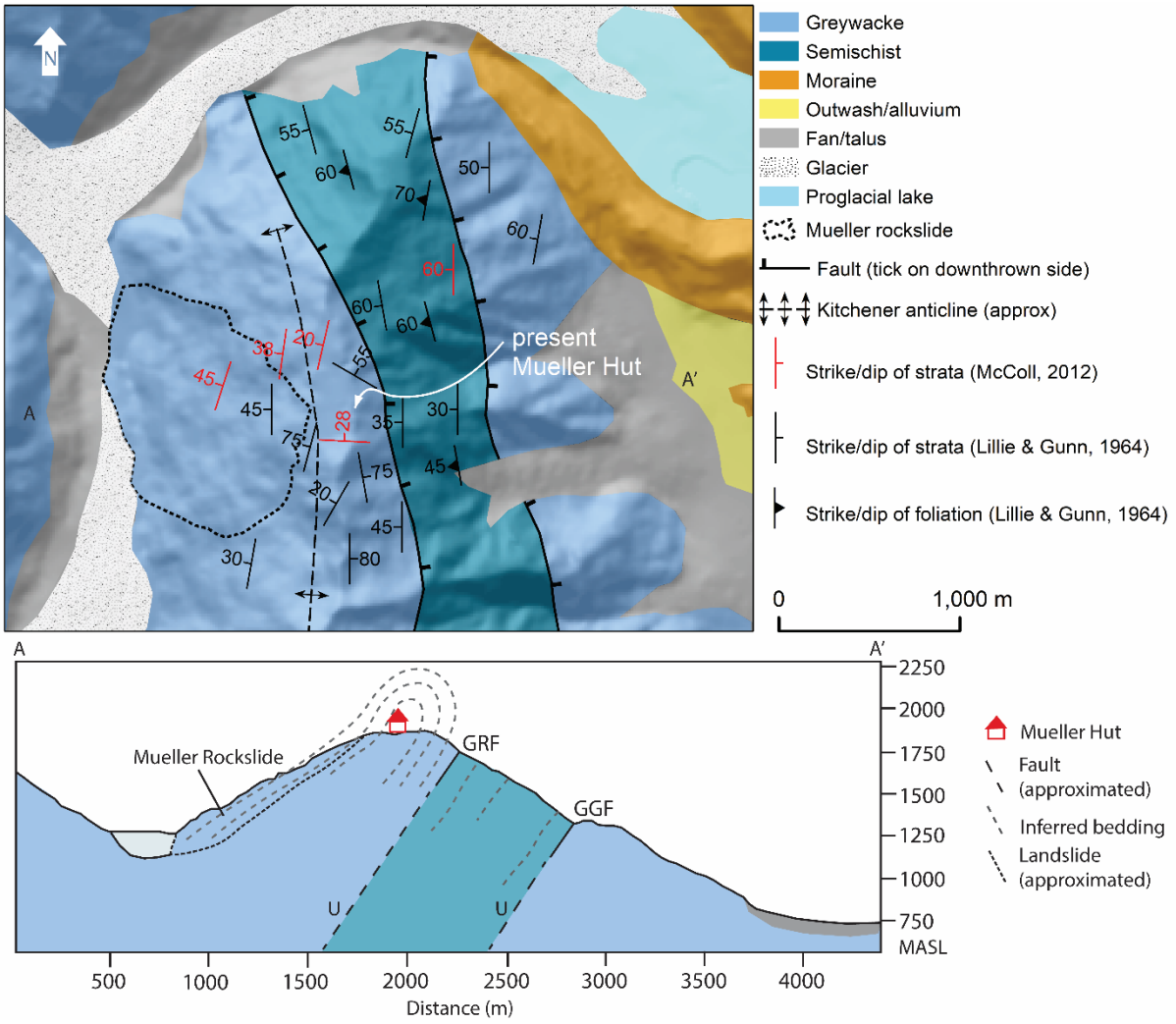

Figure 2. Geological map of Sealy Range and cross-sectional profile of the Kitchener Anticline (informed by mapping by Lillie and Gunn 1964 and McColl 2012a). Glacier extent and Mueller Rockslide outline are as mapped in this study, based on aerial imagery from 2010-2017. GRF and GGF highlight the Green Rock Fault and Great Groove Fault.

Methods

Topographic Data and Aerial Photography

High-resolution topographic data and an orthophoto mosaic were obtained using Structure-from-Motion (SfM) photogrammetry (Fig. 3) for mapping the rockslide and surrounding slopes. Photos were collected in February 2017 from a DJI Phantom 3 Professional unmanned aerial vehicle (UAV). Photos were captured from an above ground altitude of 60-120 m, in both oblique (30° from nadir) and nadir camera orientations to achieve a minimum of 75% forward and 60% side photo overlap. The SfM software Agisoft Photoscan was used to produce a dense point cloud that was decimated to a 0.25 m resolution DEM, and a 5 cm pixel-resolution orthomosaic image. The georeferencing of the SfM model was provided by 22 ground control point (GCP) targets surveyed with a Trimble R10 GPS, with a 5-km RTK baseline correction,

and referenced against the national survey network (using B8Y2 UNWIN geodetic benchmark, and the New Zealand Geodetic Datum 2000 and New Zealand Vertical Datum 2016). The GCPs were distributed asymmetrically, due to difficulty deploying them in steep, fractured terrain along the glacier and lower and southern slopes of the rockslide (Fig. 3). The Photoscan estimate of GCP vertical uncertainty was an RMSE 0.156 m. We provided an independent assessment of this modelled error by comparing the modelled DEM elevations with our own 10 independent spot height elevations measured with RTK GPS. The mean difference and RMSE we calculated were 0.35 m and 0.59 m respectively, with a maximum of 1.75 m (Table 1.) These vertical error values are mostly representative of the area inside our GCP distribution and therefore we have lower confidence in the model accuracy in the western and southern parts of the model outside of the GCP distribution. However, the combination of oblique and nadir convergent photographs will have reduced the amount of radial distortion in the model periphery, as shown by James and Robson (2014), and where GCPs were not available, the aircraft's built-in GPS (better than 10 m accuracy) provided camera positions for lens optimisation. We consider the resulting accuracy of the DEM to be adequate for the purposes intended here: to support geomorphological and geotechnical mapping of the rockslide and surrounding slopes.

Table 1. Comparison between selected spot heights and equivalent DEM elevations. Distance to nearest GCP indicates model performance away from model control points.

Spot Height ID	Spot Height Elevation (m) (NZVD2016)	DEM Elevation (m) (NZVD2016)	Elevation Difference (m)	Distance to nearest GCP (m)
1	1844.62	1844.69	0.07	16.3
2	1779.28	1779.09	0.19	14.9
3	1472.66	1472.21	0.45	11.1
4	1686.85	1686.55	0.29	54.6
5	1714.83	1714.78	0.05	17.9
6	1787.33	1787.39	0.06	11.5
7	1786.96	1786.70	0.26	37.7
8	1812.91	1812.77	0.15	112.7
9	1815.55	1815.37	0.18	35.9
10	1554.84	1556.59	1.75	99.1
Mean			**0.35**	**41.17**

Geomorphological and fracture mapping

A combination of field observations and remote-sensing was used to map the geomorphology and structures present at the site. Using the SfM hillshade model and orthomosaic, landforms and features on and around the rockslide were mapped, including scarps, major fractures, lateral moraines, and areas of debris cover and bedrock outcrop. Detailed field mapping over three consecutive summers was completed in 2017, 2018 and 2019. Features mapped in the field included scarps, fractures, tension cracks and bedding. A total of 41 bedding measurements and 206 joint measurements (including fractures and tension cracks) were taken in the field.

Mapping of discontinuity locations and orientations was done in the field at accessible bedrock outcrops on the rockslide and ridge, and along the geophysical transects (described below). Discontinuities were also measured along one to two scan-line surveys perpendicular to each geophysics transect (Fig. 3). For less accessible locations of the site, major fractures were mapped remotely using Point Cloud Viz (Mirage Technologies SL) to select fractures in 3D space using each fracture face. Discontinuities were plotted on stereonets, with pole-to-plane density contours, using the software DIPS (Rocscience, 2018), to identify orientation patterns and major fracture sets within the fracture network. Discontinuities were grouped into two structural domains; Domain 1 within the rockslide including the rockslide body and headscarp; and Domain 2 outside the rockslide and along the ridgeline. Kinematic analysis was conducted for both structural domains for plane, wedge and flexural toppling failure, with the aim of evaluating the feasibility of simple structurally-controlled failure mechanisms (following Kliche 1999). Average slope dip and dip direction obtained from the SfM derived digital surface model were used in the kinematic analysis. A friction angle of 33 degrees was taken from previous tilt test results (McColl 2012b) assuming failure along an argillite bedding surface. Argillite and siltstone beds are a common feature of the greywacke within the study area and their lower strength compared to sandstone makes them the most likely structural weakness along which bedding failure may be facilitated. This friction angle may be greater than that of a fully formed sliding surface (i.e. at residual strength) in argillite, so is treated as an upper estimate for the frictional strength of the argillite beds.

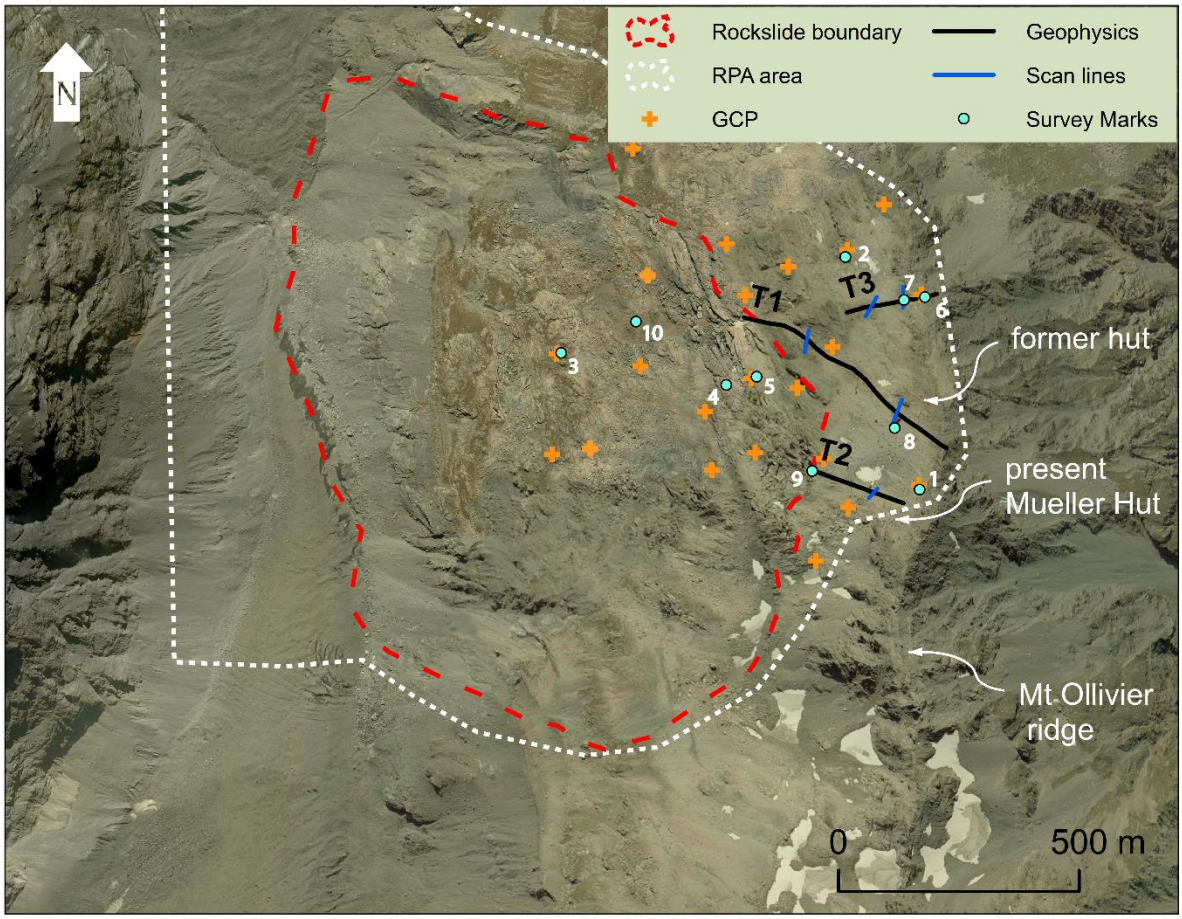

Figure 3: Approximate rockslide outline, extent of the UAV flights for photogrammetry and ground control points (GCPs), spot height survey marks used in Table 1, and the geophysics transects. Imagery is 0.75 m LINZ aerial photo (~ 2004-2010).

Geophysical surveys

Seismic Refraction Tomography (SRT) and Ground Penetrating Rader (GPR) were used to image the subsurface rock mass around the rockslide headscarp, Sealy Range Ridgeline and Mueller Hut. The steep and highly unstable topography of the landslide body made it impossible to conduct geophysical surveys along the rockslide. The geophysical surveys were used to identify rock mass discontinuities and better characterize the subsurface extent and nature of fractures, either identified or obscured by scree at the surface. In particular, the subsurface mapping was to help evaluate the potential for rockslide retrogression through identification of incipient shear surfaces east of the Mueller Rockslide crown. SRT has been previously used to investigate the internal structure of rock slope instabilities, such as the Åknes Rockslide in western Norway (Ganerød et al. 2008; Heincke et al. 2010), the slope instability at Randa in the Swiss Alps (Heincke et al. 2006), the La Séchilienne Rockslide in the French Pre-Alps (Meric et al. 2005) and several rockslides in Tien Shan, Kyrgyzstan (Havenith et al.

2000; Havenith et al. 2002). GPR has been used in previous rockslide and rock fall studies to investigate individual fractures and discontinuities (Toshioka et al. 1995; Theune et al. 2006) as well as stratigraphic analysis (Davis and Annan 1989). Here we combine both methods to maximise the potential information produced regarding shallow (<20 m) subsurface rock mass conditions.

3 combined geophysics transects using SRT and GPR were deployed along Sealy Ridgeline in a roughly east-west direction (T1-T3 in Fig. 3), targeting major fractures visible at the surface, and where possible, following accessible bedrock outcrop. In addition, 3 GPR transects were completed in the immediate area of Mueller Hut (Fig. 3). Transect 1 (Mueller Hut transect) extends from the eastern Sealy Range ridgeline, past the present-day Mueller Hut to the main rockslide headscarp. Transect 2 (Mount Ollivier transect) is located farthest to the south, stretched east-west along the northern slope of Mount Ollivier. Transect 3 (Old Hut transect) is nearer to the northern end of the rockslide and stretches from eastern Sealy Range ridgeline near the former Mueller Hut, west to the rockslide headscarp. SRT was completed using repeated overlapping transects of 24 geophones. Transect 1 had geophone spacing of 6 m and consisted of 4 overlapping transects (each 138 m long) resulting in a total length of 531 m. Transects 2 and 3 had a geophone spacing of 8 m with 3 additional offset shots after geophone 24 resulting in a total transect length of 204 m. Different geophone spacing resulted in different resolutions for the seismic tomographies which range from 1.5 m at T1 to 2 m at T2 and T3.

Seismic waves for the SRT survey were generated by sledgehammer shots between each geophone and three offset shots before or after the first and last geophone. Five shots were stacked to increase signal-to-noise-ratio. Geophone and offset shot positions were recorded using a Trimble R10 RTK DGPS and implemented in the data processing using Reflex W 7.0 (Sandmeier 2012). First arrivals were picked manually. Raw data analysis was performed using the approach by Krautblatter and Draebing (2014). The raw data were inverted using the SIRT algorithm of Reflex W and ray path tracing was performed to check ray coverage. The quality of the final tomographies was calculated and total absolute time difference (3.96 – 4.72 ms) and root mean square error (5.58 - 6.27 ms) are in an acceptable range of 1/4 of the seismic wave amplitudes at Mueller Rockslide (10 to 20 ms).

The volumetric fracture density (P_f) for the rock mass was calculated using the equation by Clarke and Burbank (2011) and is expressed as a percentage:

$$P_f = \frac{V_f}{(V_r - V_f)}\left(\frac{V_r}{V_p} - 1\right)$$

where V_p is the subsurface p-wave velocity measured by the seismic survey, V_r is the intact rock velocity, and (V_f) is the velocity of the fracture material. Rock samples collected from the field were cut into 6.27 cm wide and 4.5 to 5.8 cm long cores and used to quantify V_r in the lab in parallel and perpendicular directions. A Geotron ultrasonic generator USG40 in combination with Geotron preamplifier VV51 and 350 kHz sensors generated the seismic signal. Seismic signals were recorded using a PICO oscilloscope and data analyzed using the software Geotron Lighthouse UMPC. Intact rock p-wave velocity (V_r) is 0.54 ±0.4 km s^{-1} and anisotropy on rock core scale according to Draebing and Krautblatter (2012) is 6 to 8 %. We assumed that the fracture infill is air and, therefore, V_f is the velocity of air (0.33 km s^{-1}).

Ray path tracing was performed to estimate fracture location and persistence using the technique developed by Phillips et al. (2016). Ray density indicates the number of rays crossing a 1.5 x 1.5 m rock column within seismic transects. P-waves travel along layer boundaries (Hauck and Von der Mühll 2003) which can be different layers of rock mass with different elastic properties or anisotropies caused by macroscopic air-filled faults and joints (Heincke et al. 2006). Therefore, ray density is increased in areas of fracturing in comparison to areas of low fracturing.

To assist with SRT interpretation, and to identify major sub-vertical fractures, faults, and bedding structures, ground penetrating radar reflection surveys were conducted at each seismic transect using a Sensors and Software Pulse Ekko Pro GPR. Three additional GPR transects were deployed around Mueller Hut (GPR 1, 2, 3 in Fig. 3) to evaluate the subsurface persistence of several scarps. They are 30, 55 and 100 m long respectively. For all GPR transects, stepped measurements were taken at 25 cm intervals along each transect using 100 MHz unshielded antennas. Topographic profiles from RTK GPS surveying were applied to correct for topography, and velocity was evaluated from hyperbola-fitting and common mid-point surveys and applied in Sensors and Software Ekko Project 3 software. Gains were adjusted to enhance weaker reflectors, using a combination of SEC2 and AGC methods. Discontinuities were mapped onto the radargrams, guided by matching discontinuities seen in the radargram with those observed in the field.

Subsurface features were identified to a depth of 15 m within the GPR radargrams and up to 20 m in the seismograms. These penetration depths are deemed adequate for identifying surficial rock mass quality around the ridgeline and Mueller Hut as well as identifying a potential sliding surface within the headscarp / toppling zone.

334

335 **Rock Mass Characterisation**

336 Descriptions of the rock mass and rock mass characterization were made for the rockslide and
337 surrounding area. The Geological Strength Index (GSI) was utilized to describe rock mass
338 "blockiness" and the presence of discontinuities within the rock mass following the
339 methodology of Marinos et al. (2005).

340

341 **Slope Stability Modelling**

342 To help evaluate the importance of rock mass anisotropy (i.e. bedding) in influencing the
343 stability conditions and development of the Mueller Rockslide, we used the two-dimensional
344 finite element software RS2 (Rocscience 2019). A cross-section equivalent to that shown in
345 Figure 2 was used to set the topographic boundaries of the model. The assumed geomechanical
346 properties (Table 2) were selected to be representative of greywacke in New Zealand
347 (compilation in Cook, 2001) and conditions observed at the Mueller Rockslide. Equivalent
348 elastic perfectly plastic Mohr-Coulomb strength parameters were estimated using RocLab
349 (Rocscience, 2017). To evaluate the influence of the bedding orientation on the displacement
350 and stability condition at Mueller Ridge, a model with isotropic strength material (no bedding)
351 was compared with a model assuming an anisotropic direction 40° dipping to the west
352 (bedding). The frictional strength along the anisotropy plane was assumed to be 33° using the
353 tilt test results from McColl (2012b). The critical shear reduction factor (SRF; Matsui and San
354 1992) was calculated to assess the relative stability of both the isotropic and anisotropic models.

355

356 Table 2: Summary of geomechanical parameters used in the exploratory finite element models
357 of the Mueller Rockslide.

Property	Value
Density	2600 kg/m^3
Intact rock Young's modulus	35 GPa
Poisson's ratio	0.25
Unconfined compressive strength	80 MPa
Geological strength index	60
mi	11

358

359

360

361

362 **Results**

363 **Rockslide geomorphology**

364 From our mapping, we divide the rockslide and surrounding slope into three major zones,
365 characterised by distinct morphology: 1) a main landside body, 2) a complex headscarp zone
366 of block toppling, block dilation and sliding, and 3) a retrogressive zone with large tension
367 cracks, fractures and small scarps.

368

369 *1) Rockslide body*

370 The main rockslide body is expressed as a partly disaggregated rock mass that has been moving
371 downwards and outwards into Mueller Glacier Valley (Fig. 4). Extending from 1700 to 1150
372 m.a.s.l., the surface of the main rockslide body slopes towards the valley floor at an inclination
373 of approximately 31˚; the upper slope averages 29 to 30°, steepening to 37-39° near the
374 rockslide toe. This transition is marked by a lateral moraine extending across the majority of
375 the landslide. Much of the rockslide body is mantled with debris from weathering processes,
376 rockfall, glacial deposits, and blocky debris from disaggregation of the rockslide body. Where
377 not covered by debris, the bedrock shows indications of sculpting by glacial or nival erosion
378 (smoothed rock surface and striations), and evidence of brittle deformation (fractures, and
379 scarps). Most of the scarps within the rockslide body are downslope-facing, but in the upper
380 part of the rockslide body there is a low-profile upslope-facing scarp, which is hypothesised to
381 form the downslope edge of a large graben structure (Fig. 4) which was identified in field
382 mapping. The graben structure may represent the separation of the rockslide body from the
383 headscarp zone but has little to no vertical geomorphic expression because it is mostly filled
384 with blocky debris from the collapsing headscarp zone.
385 A prominent lateral moraine can be traced across the rockslide body immediately above a
386 prominent break in slope 160-230 m above the Mueller Glacier surface (Fig. 4). Up- and down-
387 valley of the rockslide boundary other lateral moraines were identified, some resting at higher
388 and more eastward locations on the slope. It is inferred that the moraine ridges identified in
389 Figure 4 outside the rockslide boundary are of equivalent (LIA) age to the moraine ridge on
390 the rockslide body. If correct, rockslide movement has displaced the lateral moraine on the
391 rockslide by about 100-130 m horizontally west and 110-120 m vertically down.
392 The toe of the rockslide body below the LIA trimline is affected by shallower mass movement
393 processes, with an apron of debris having built up at the base of the slope. At the southern end

of the rockslide toe, and beyond the rockslide extent, shallow mass movement processes have removed parts of the LIA trimline and moraine altogether.

2) Headscarp and toppling zone

The crown of the rockslide is defined by a network of stepped, discontinuous and echelon scarps that form a wide (200-300 m) headscarp zone extending from 1830 to 1700 m.a.s.l. Slope angle varies from <30° in areas of intact bedrock to 90° along fractures. Individual scarps have vertical offsets of up to 20-30 m (Fig. 4). The visible cumulative vertical displacement across these scarps is 55-70 m in the northern/upper section of the headscarp and decreases to 30-40 m in the southern part where the scarp transitions into a single arcuate scarp and becomes the southern lateral boundary of the rockslide. Towards the north, the headscarp is less defined but appears to transition into a lateral scarp that defines the northern extent of the rockslide. The lateral scarp is 50-100 m high, and of varying strike, appearing to follow planar pre-existing structures. The stepped scarps forming the headscarp are facilitating forward-toppling of large (up to 140 m long, ~0.2 Mm^3 in volume) blocks of rock (Fig. 4). Several incipient block topples/failures are evident from the presence of open cracks. It appears that rock blocks have been breaking up and delivering blocky debris to the main rockslide body.

3) Retrogressive zone

Above the crown (>1830 m.a.s.l.) the slope gradient decreases to <10° and is represented by an almost flat-topped ridge heavily mantled with blocky scree, with patches of exposed fractured bedrock. Fractures vary in aperture from tight to the largest open fracture being over 3 m wide to a depth of at least 7 m. Fracture length varies from several metres long to some fractures that extend for over 100 m along the ridgeline. Several large tension cracks (without evidence of vertical displacement) are present. These vary in width from 0.2 m wide to 3m and extend for over 20 m. Smaller tension cracks measured 0.02 to 0.2 m wide and up to 10 m long. While most fractures have no evidence of shearing, some have evidence of vertical displacement represented by low scarps (Fig. 4). This vertical displacement varies from 0.5 m to 2 m, extending for tens to hundreds of meters with down-throw towards the SW and SSW. They are often subtly visible in the field where mantled by debris but are more readily recognised and traceable in the DEM hillshade and aerial photography. Where the scarp travels through bedrock, extensive dilated fracturing occurs with some fractures exceeding 2 m in aperture. The scarps are at a similar orientation to the major scarps making up the headscarp

zone below the rockslide crown; for example, the southern-most scarp trends northwest and dips southwest through the northern face of Mount Ollivier before intersecting the headscarp zone (Fig. 4). To the north, two scarps at similar orientation to the southern-most scarp are located on each side of Mueller Hut and converge 100 m north-west of the hut. Both have subtle surface expression but at their point of intersection there is an area of intense fracturing approximately 30 m long, 1-3 m wide and 1-3 m deep before becoming scree filled.

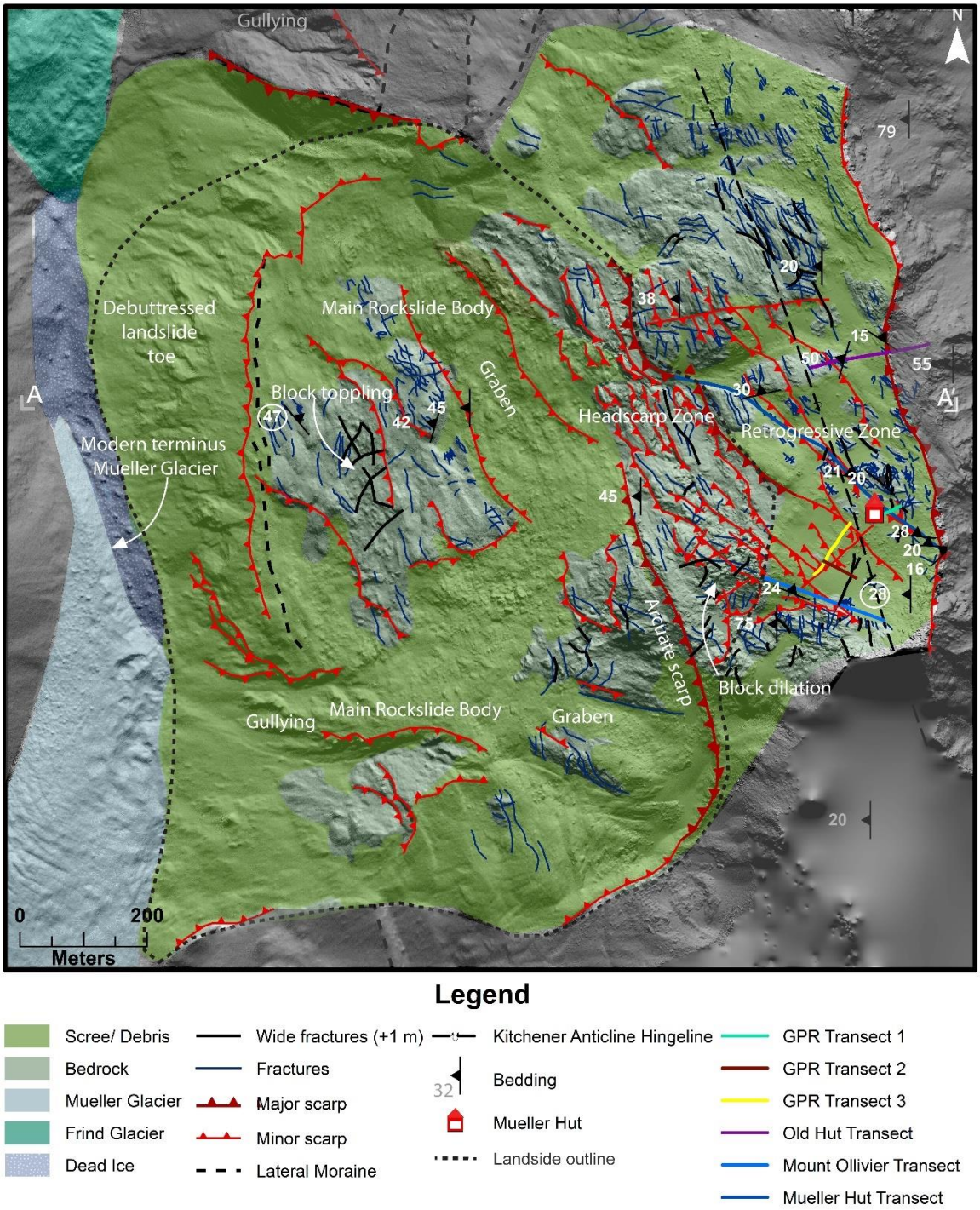

Figure 4. Geomorphic map of the Mueller Rockslide. Mapped bedrock (light green) can be seen throughout most of the ridgetop and headscarp but is limited to a central zone with the rockslide. The majority of the rockslide is debris-mantled (darker green). Major and minor scarps are located throughout the rockslide with additional scarps identified and located throughout the ridgetop to the east of the main rockslide headscarp. GPR and SRT transects are located near Mueller Hut and extend generally E-W and NE-SW. At the northern end of the rockslide, Mueller Glacier has almost thinned completely, allowing the Frind Glacier to

flow up valley back towards the rockslide. A to A' highlights the location of the cross section shown in Figure 12. Circled strike and dips are not considered in situ (i.e. have been significantly displacement by landslide movement).

Rock Mass Characterisation

The greywacke sandstone is typically weathered orange (lightly weathered, NZGS 2005) with fresh surfaces light grey. Jointing is obvious and quartz veins often fill many open joints with some being over 10 cm wide. Geological Strength Index (GSI) was used to describe the sandstone rock mass quality as very blocky with good surface which represents a GSI range between 50 and 60. The rock is indurated and takes several hard hammer or sledge hammer blows to break. Minor seepage could be seen within the main headscarp zone. Siltstone and argillite bedding within the study area is often dark grey, laminated and highly fractured with small very angular blocks. The argillite rock mass is intensely jointed with fair surface condition and can be broken by hand with effort. The argillite rock mass is considered as blocky, disturbed and seamy which corresponds to a GSI of between 30 and 40.

Discontinuity Analysis

Stereographic projections of discontinuity orientations are presented as well as kinematic analysis for planar sliding, wedge and flexural toppling (Fig. 5). Discontinuities are grouped into two structural domains 1) ridgetop / retrogressive zone (Fig. 5) and 2) headscarp and rockslide body zones (Fig. 6) with several discontinuity sets identified within each domain. Identified discontinuities are divided into bedding, joints and faults.

Seven discontinuity sets are identified within the retrogressive zone (Fig. 5a). R1 is a strongly defined bedding set dipping north with an average dip of 30°. R2 is a near vertical joint set trending north-south and dipping predominantly to the west from 80°–90° although several joints dip steeply to the east. R3 is a minor joint set dipping steeply north at 85°. R4 is a minor joint set striking east-west and dipping at approximately 50° to the south. R5 strikes northwest and dips steeply to the southwest at 75°–90°. R6 strikes north-south, similar to R2 but with a shallower dip of 60°-70° to the west. R7 strike northwest like R5 but dips east at 70°-80°.

Discontinuities mapped within the rockslide body and headscarp differ from those identified along the ridgeline (Fig. 6a). In total 5 discontinuity sets are identified. L1 is a predominantly defined by bedding, dipping to the west from 30°-70° with an average dip of 50°. L2 is a minor joint set again strongly defined by bedding although this set dips to the north-west at approximately 45°. L3 strikes northwest and dips to the south-west at 80°. L4 is an east-west

trending joint set, similar to R2 in orientation with joints dipping to the west with an average dip of 80° to 85°. L5 is a minor joint set dipping to the south-east at approximately 80°.

Kinematic analysis was conducted for both domains, to explore potential differences in kinematics between the upper and lower part of the slope. We assessed the potential for planar, wedge, and toppling failure under the following scenario: an empirically-derived friction angle of 33° for the mudstone, and a slope dip and dip direction of 40/270. The direction (of 270°) is along the steepest path of the slope, and is slightly oblique to the dip direction (~285°) of most bedding measurements. Using an average slope angle of 31° (which is below the friction angle of 33°) does not result in kinematic feasibility by planar failure. However, slope angles of up to 39° were measured at the toe, and we evaluate the kinematic feasibility at a slope angle of 40° to provide a conservative estimate that allows some freedom for a potentially lower friction angle.

For the retrogressive zone (Domain 1), the kinematic analysis shows that potential for planar failure is minor (Fig. 5b) with only one bedding point (3.8% of total bedding measurements) falling within the failure envelope. Wedge failure analysis shows the potential for failure along the intersection of R3-R6 and R4-R6 joint sets (Fig. 5c), however, the failure envelope falls just outside the definitive intersection of these joint sets. Flexural toppling analysis shows potential toppling along the R4 eastward dipping discontinuities (Fig. 5d).

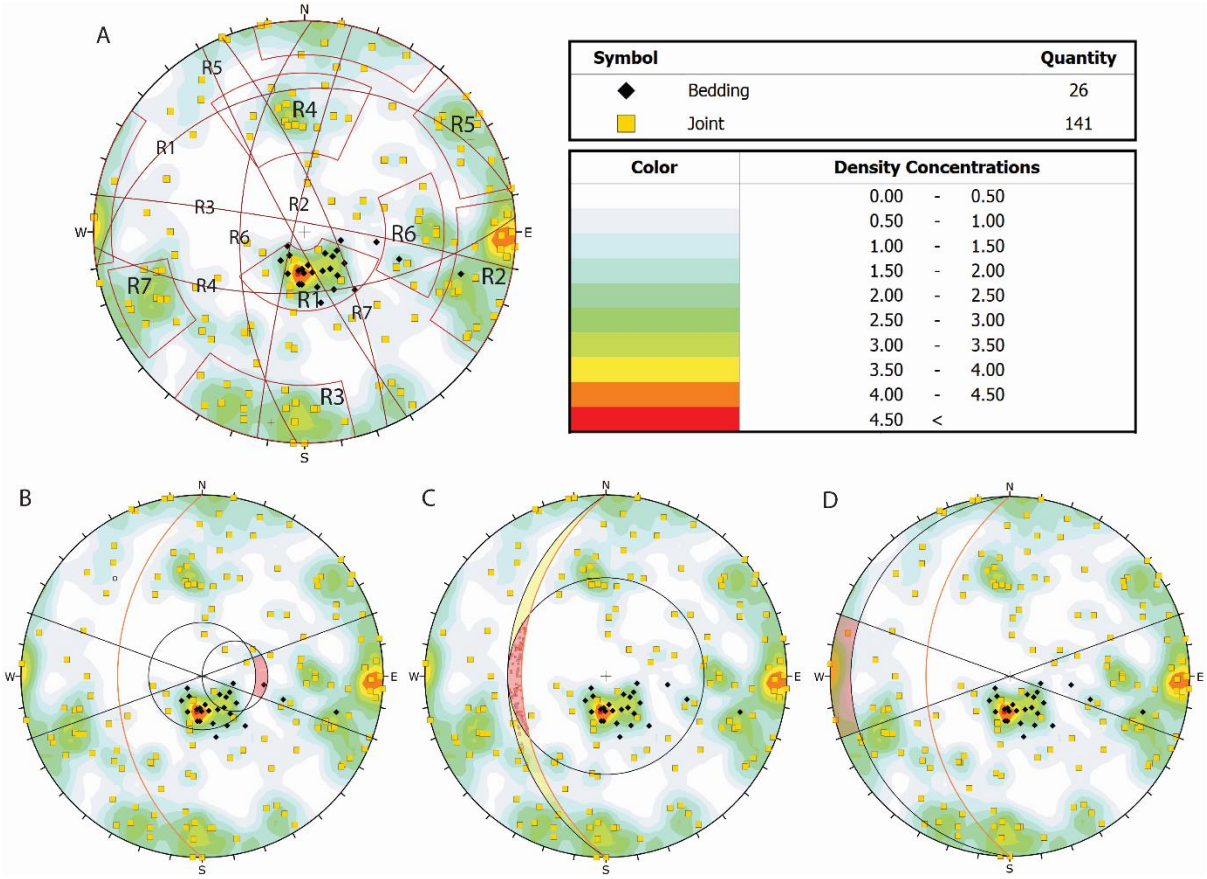

Figure 5. A) Joint sets (R1-R7) and corresponding planes for discontinuities within the retrogressive development zone of the rockslide. Kinematic analysis was completed for planar sliding, wedge and flexural toppling respectively (B, C, D).

For Domain 2, the kinematic analysis showed marginal potential for planar sliding although no discontinuities fall in the failure window; several L1 discontinuities are at the margin or just outside of the failure window. Wedge failure analysis shows potential for L1-L3 and L1-L5 intersections within or just outside the failure envelope (Fig. 7c) (2.2% within failure window). Flexural toppling analysis shows L4 discontinuities falling within the failure envelope when the slope angle is 40° (Fig. 7d) (1.3% total discontinuities and 16.7% of L4 discontinuities).

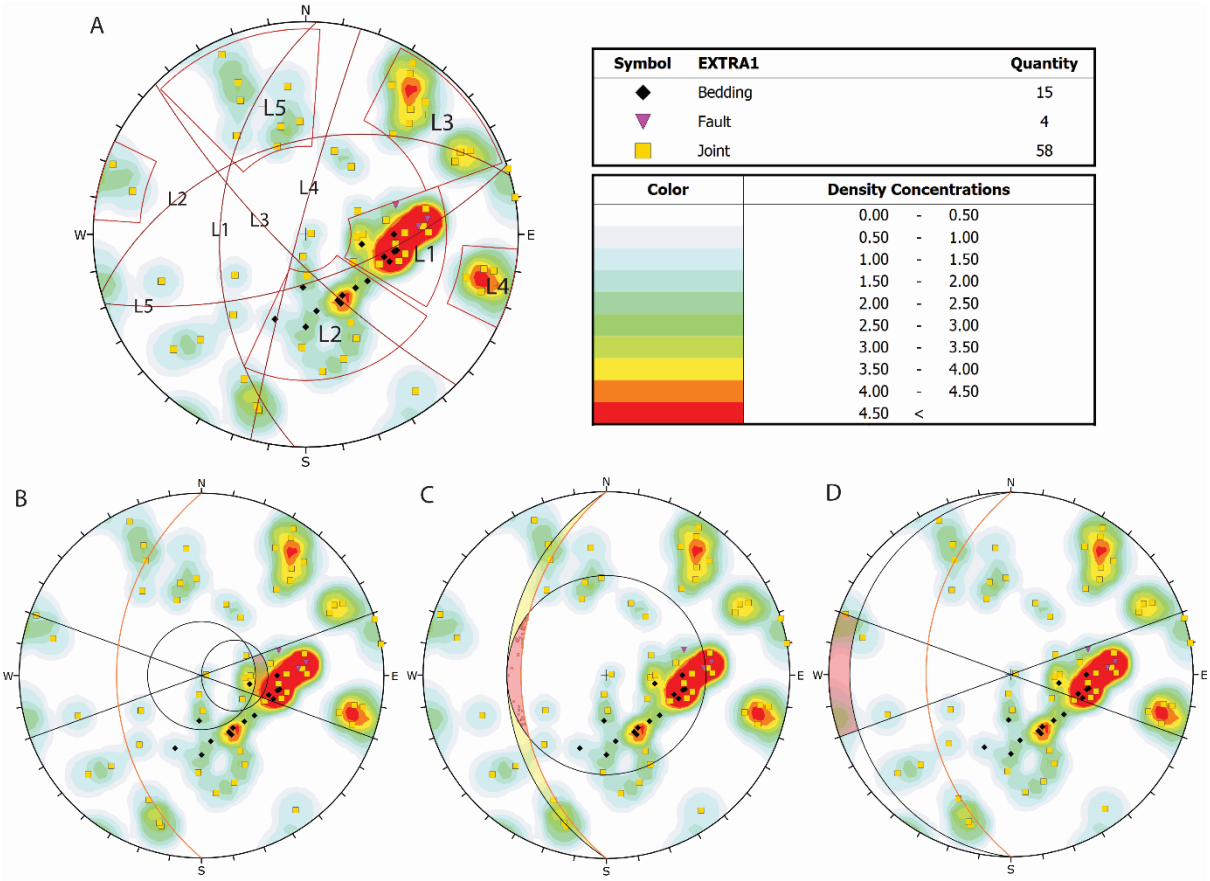

Figure 6. A) Joint sets (L1-L5) and corresponding planes for discontinuities within the landslide and headscarp zone of the Mueller Rockslide. B-D) Planar, wedge and flexural toppling kinematic analysis respectively.

Subsurface data: SRT and GPR

Mueller Hut Transect (T1)

The Mueller Hut transect (T1) extends from 100 m east of Mueller Hut in the upper ridge to the rockslide crown for a total length of 500 m (Fig. 4). There are three distinct velocity layers recognizable along the seismic transect (Fig 7.). The near-surface p-wave velocity layer (0.5-0.95 km s^{-1}) is predominantly located within the first 100 m of the transect to a depth of 5 to 7 m below ground level and from 140 m to 380 m to a depth of 3-5 m. A second, faster, velocity band (0.95 to 1.7 km s^{-1}) is observed predominantly from 140 to 380 m, through localized areas of bedrock outcrop and in the final 150 m of the transect towards the rockslide crown. The third and fastest velocity band (>1.7 km s^{-1}) is found between 400 and 480 m along the transect. Fracture density results show high values in the first 100 m of the transect as well as between 140 and 280 m, coinciding with the low p-wave velocities outlined above and areas of blocky debris seen on the surface. Fracture density decreases rapidly with depth under areas of scree and in areas of bedrock from 30-50% in scree zones to 10-30% in bedrock and the underlying

rock mass. The last 150 m of the transect shows lower fracture densities particularly in relation to the debris-mantled ridgeline.

Ray density analysis shows the percentage of rays per 1.5 x 1.5 m grid spacing with high ray density indicating the presence of linear features or discontinuities. In the first 100 m, of the transect, ray density appears to be related to scree, and suggests an absence of large, persistent fractures within the bedrock. Farther down the transect, high ray densities are detected from 140 to 280 m with increased ray density at the surface and moderate density at depth to ~30 m indicating the presence of large, persistent structures (black arrows in Fig. 7b). High ray density also indicates a large persistent fracture at 430 m is also indicated by high ray density.

The corresponding GPR profile for Transect 1 is 400 m long, extending almost to the rockslide crown. Evidence of bright reflectors which coincide with areas of bedrock at 100-200 m are interpreted as bedding planes. Reflectors with a similar signature can be seen at depth at 175 m along transect and at 380 m (Fig. 7c, d). The first 210 m of the transect which bypasses Mueller Hut also shows extensive orthogonal fracturing with apparent dips to the east and west. A highly fractured zone from 140 m to 210 m along the transect is marked by significant fractures which extend for ~8 m through the GPR profile. A scarp identified in the geomorphic mapping and in the field at 140 m is hard to identify within the GPR transect due to both being oriented in a north-west direction however there is evidence of shear planes and displaced bedding around 140 m.

From 210 m to 310 m, fractures appear to dip predominantly westward as the transect moves towards the crown of the Mueller Rockslide. A highly fractured zone can be seen between 220 m and 245 m (Fig. 7c) which coincides with where the two minor scarps either side of Mueller Hut intersect and with several large fractures identified on the geomorphic map. Bright linear reflectors identified between 290 m and 320 m are interpreted as bedding. From 310 m, fractures have an apparent dip to the east, coinciding with the transition to block toppling as the transect nears the headscarp.

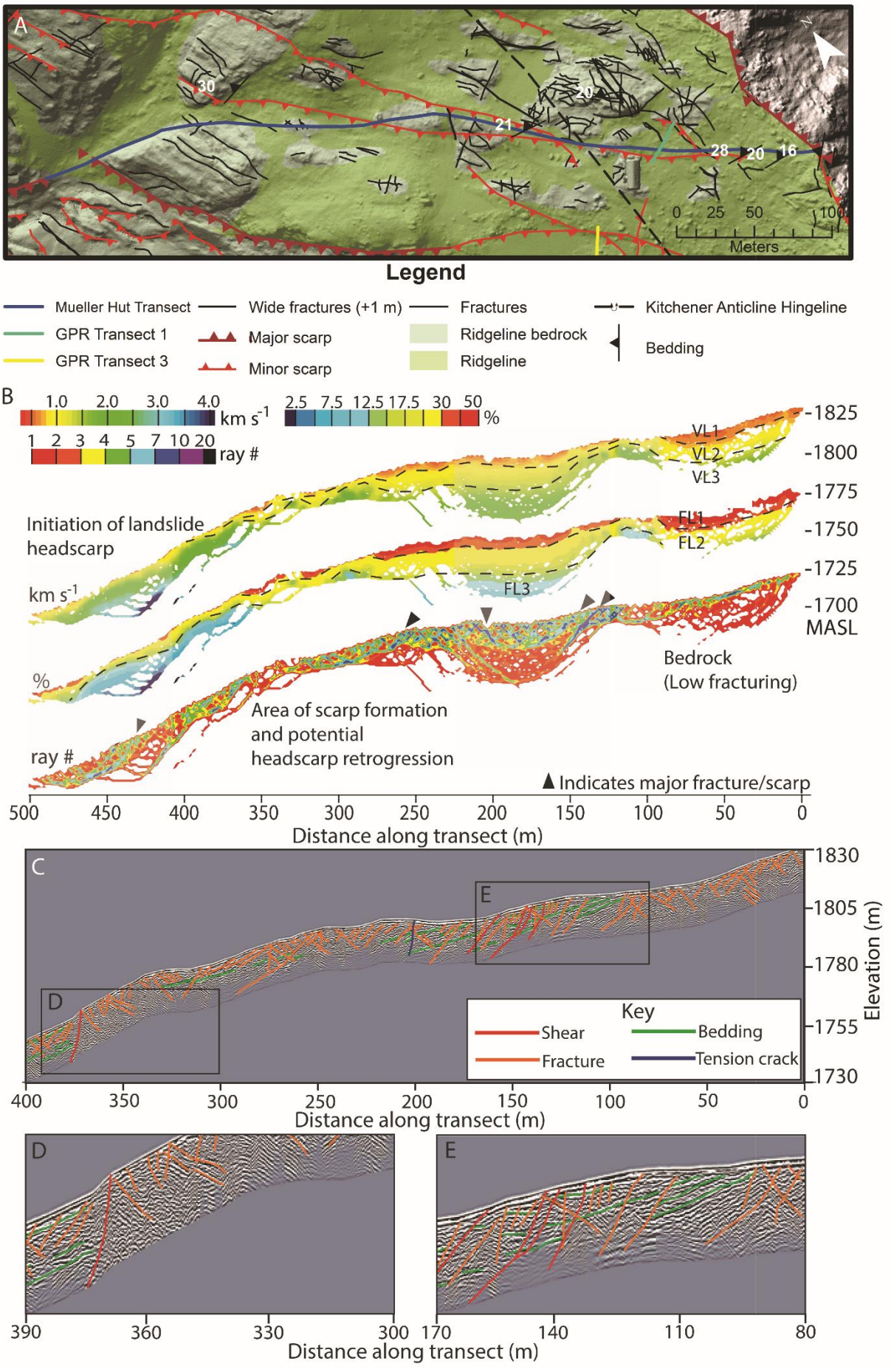

Figure 7. Mueller Hut seismic transect (T1). A) Geomorphic map of the transect. B) SRT transect consisting of P-wave velocity, fracture percentage and ray density. High ray density indicates clustering of linear features (black arrows) indicating potential scarp or fracture development. C) GPR transect for 0 – 400 m. D) Beginning of the block toppling and headscarp zone. E) GPR directly adjacent to Mueller Hut (105m).

Mount Ollivier Transect (T2)

The Mount Ollivier transect (T2), located south of Mueller Hut, is 200 m long extending from below Mount Ollivier to the rockslide headscarp (Fig. 4). Two p-wave velocity layers have been identified within the Mount Ollivier Transect (Fig. 8). The first (0.5 to 0.95 km s^{-1}) is located mainly in the top 10 m through the entire transect extending to 15 m depth from 120-160 m (Fig. 8b). The second, and faster, velocity band (0.95 to 1.7 km s^{-1}) is found from 40 to 160 m. A third velocity layer (>1.7 kms^{-1}) can be seen in isolation from 25 to 40 m.

Fracture density analysis shows the majority of the top 7 m of the transect shows fracture densities greater than 40% with this decreasing to 15-30% underneath the upper scree areas. At 30 m low fracture densities of less than 10% are seen, corresponding with mapped bedrock along the surface of the transect. Ray density analysis shows an area with extensive and persistent fractures at 110 to 190 m (black triangle, Fig. 8b).

The Mount Ollivier GPR transect shows an apparent dip to the west of several strong reflectors (Fig. 8c). At 55 m and 150 m are east-dipping reflectors which extend for over 10 m depth in the GPR profile. A similar albeit small feature is identified at the end of the transect between 160 and 180 m within 20 m of the previously identified rockslide headscarp. Four strong sub-horizontal reflectors are identified in the eastern most extensive feature from 22 m to 55 m, interpreted as (argillite) bedding, consistent with outcrop observations; similar but more steeply-dipping reflectors are identified between 120 and 160 m. A large tension crack (Fig. 8c, 8e) extends throughout the transect as well as extending for a total of 40 m to the north (Fig. 8a). An extensive shear plane can be seen from 110 m which extends throughout the GPR transect and is represented at the surface by a continuous 1-2 m southwest dipping scarp (Fig. 8c, 8d).

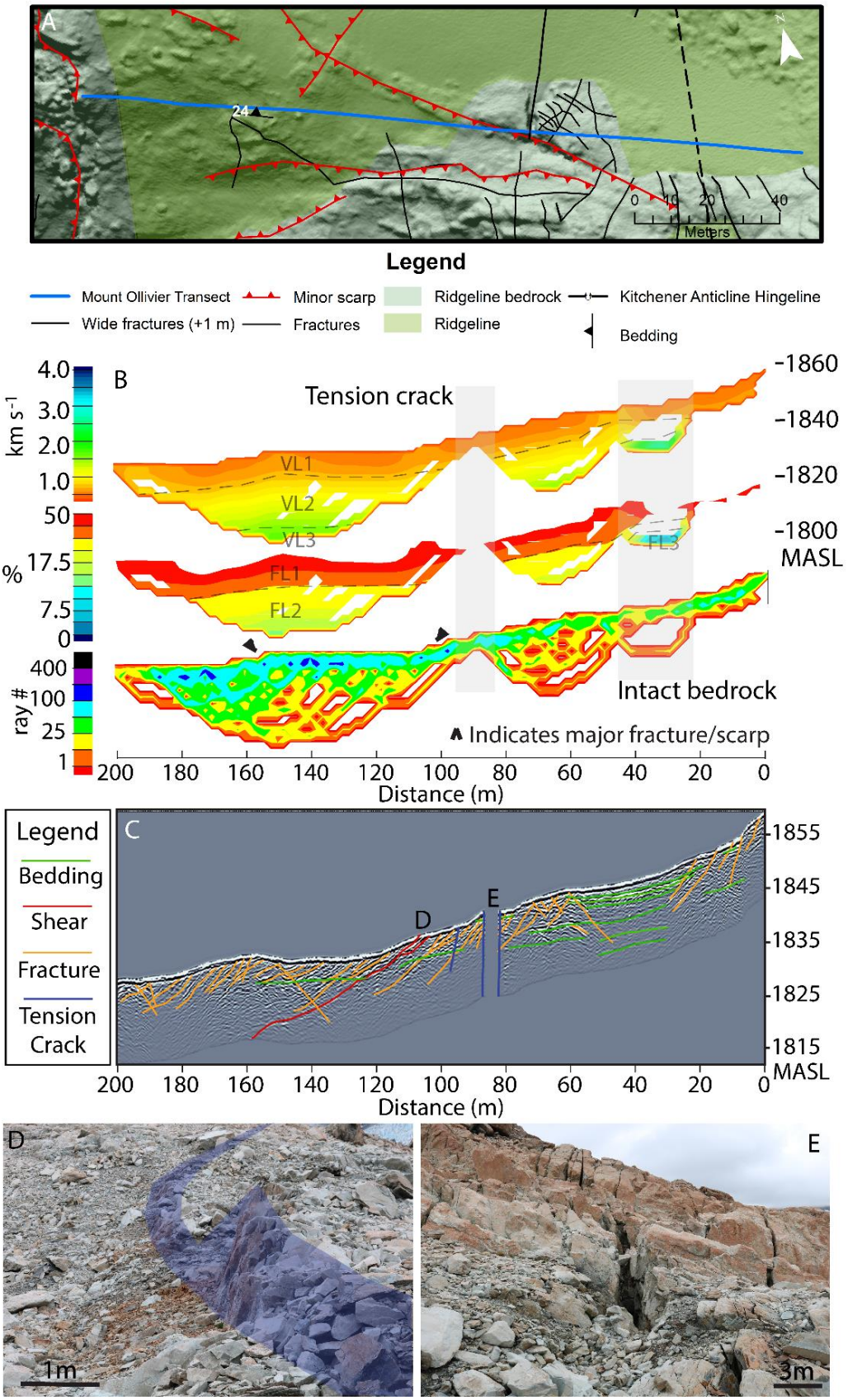

Figure 8. SRT and GPR for the Mount Ollivier Transect. A) Geomorphic map of the Mount Ollivier transect. B) SRT showing in order P-Wave velocity, fracture percentage and ray density. C) GPR with identified bedding, fractures, shear planes and tension cracks. D) Scarp

associated with the mapped shear surface within the transect dipping to the southwest (left in the image). E) Large dilated tension crack within the transect.

Old Hut Transect (T3)

The Old Hut transect (T3) is located to the north of Mueller Hut extending for 200 m from the eastern headscarp through the ridgeline (Fig. 9). P-wave velocity analysis has identified 3 dominant velocity bands. The first, and slowest, velocity band (0.5 to 0.95 kms^{-1}) is found through the upper 1-4 m depth of the majority of the transect particularly in areas mapped as debris or scree. The second band (0.95 to 1.7 kms^{-1}) is at 30 m from 0 to 12 m deep, at 70 m from 2 to 15 m deep and 160 m distance from 5 to 17 m deep (Fig. 9b). The third and fastest p-wave velocity band (>1.7 kms^{-1}) can be found from 0 to 10 m, 40 to 60 m and 80 to 150 m. Fracture density patterns show fracture zones at 30, 70 and 160 m distance display very high fracture densities of greater than 30% with the fracture zone at 70 m exceeding 50% fracture density (Fig. 9b). This fracture zone is characterized by fracture widths at the surface of greater than 0.5 m. At 150 m, both methodologies identified a large fracture zone which also corresponds to high ray densities that the existence of persistent fractures.

GPR results again have highlighted an extensive network of fracturing. Due to the blocky surface in this area and lack of outcrop, identified fractures are mainly isolated to the first 100 m of the transect near the main eastern scarp, and to an isolated but highly fractured bedrock zone from 130 to 170 m (Fig. 9e). The most extensive zone of fracturing is located from 25 m to 70 m marked by several crossed eastward and westward dipping fractures and one major failure zone (Fig. 9e; red lines) which extends through the GPR profile, marking the headscarp of the eastern rift/graben. Although graben is block filled, vertical displacement of ~5 m is estimated from the GPR profile, consistent with the height of the graben scarp. Minor fracturing from 90 to 130 m in the GPR profile is hidden in the field, the area covered with blocky debris. Strong gently-west-dipping, reflectors through this zone are interpreted as bedding which extends from 85 m to 135 m along the transect. Bedrock outcrop from 130 m to 170 m largely consists of minor superficial fracturing with fractures appearing to only extend for several

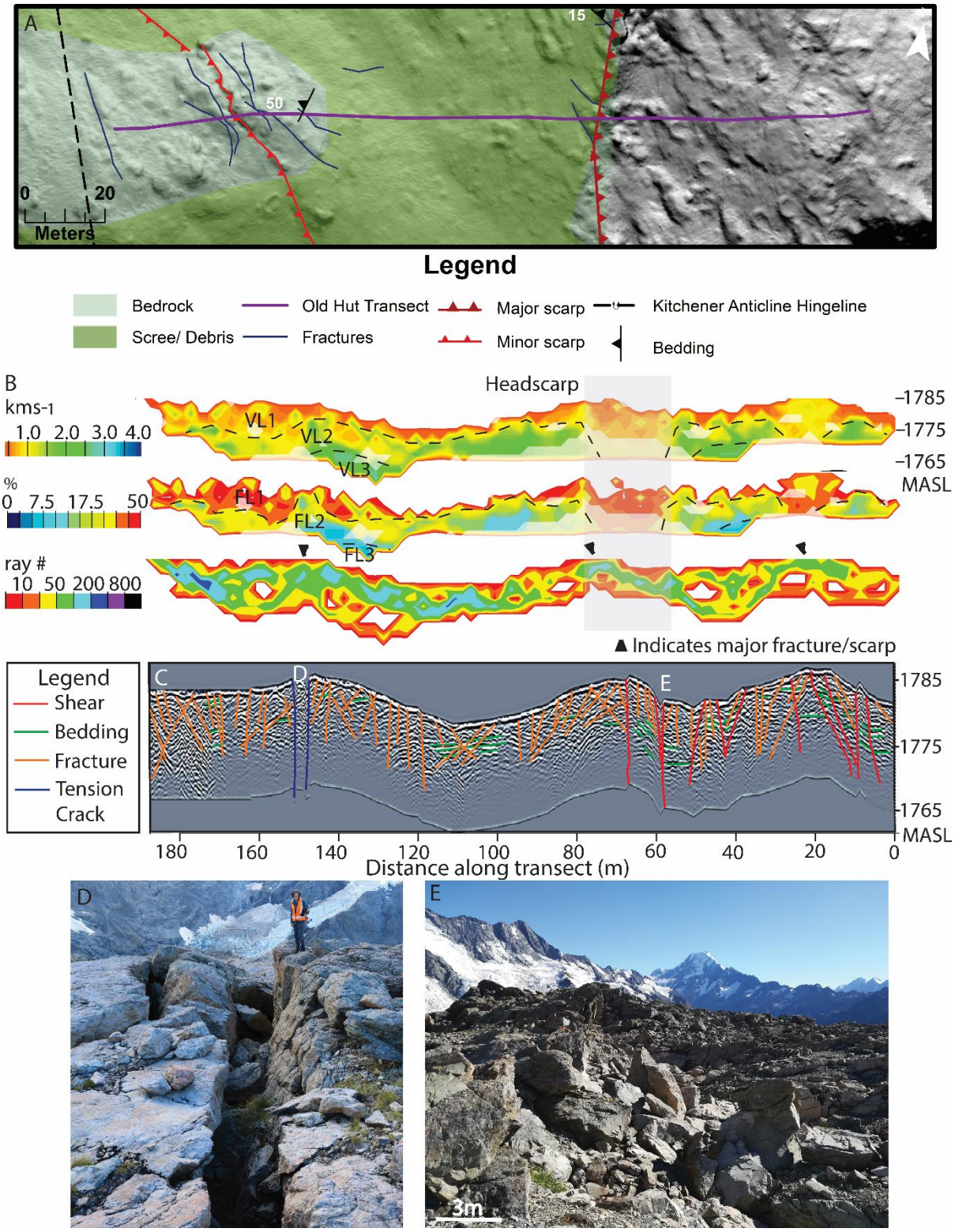

Figure 9. Old Hut seismic transect. A) Geomorphic map of the transect and surrounding area. B) SRT showing P-wave velocity, fracture percentage and ray density. C) GPR. D) Large tension crack 150 m along the transect. E) Headscarp for the eastern slope failure which is partly obscured by block fill.

meters. However, from 155 m to 165 m there two very large parallel vertical dislocations extending through the radargram and marked at the surface by two large (~30 m long and 0.5 m to 3 m wide) open fractures with a bedrock wedge in between. The wedge sits 2 m lower than the surrounding bedrock and the surfaces corresponding to the dislocations extend for at least 10 m deep in the radargram. There is no obvious vertical displacement between each side of the wedge (i.e. no scarp).

Additional GPR Transects

Radargrams from the three additional GPR transects, in proximity to Mueller Hut, are presented in Fig. 10. Transect 1 reveals the scarp identified at the surface is associated with two near vertical shear surfaces that extend through depth of the transect (Fig. 10a). Several near vertical fractures can be identified within the graben between the two shears while fractures outside the graben appear to have a shallower dip.

Transect 2 crosses a large north-south trending scarp as well as the large tension crack identified in the Mount Ollivier seismic transect. The tension crack appears to split into at least two large fractures at depth (Fig. 10b). Distinct bedding can be seen dipping to the right (west) before being displaced by an obvious shear surface which corresponds with the scarp at 45 m.

Transect 3 shows mapped scarps in the area south of Mueller Hut correspond with shear surfaces at depth. In total, 4 scarps were identified with all scarps corresponding with shear surfaces at. An additional 3 shear surfaces were identified which do not correspond to scarps at the surface (Fig. 10c). Determining the depth of these shear surfaces was difficult due to the poor quality of the GPR in the final 50 m of the transect however all extend to at least 10 m depth.

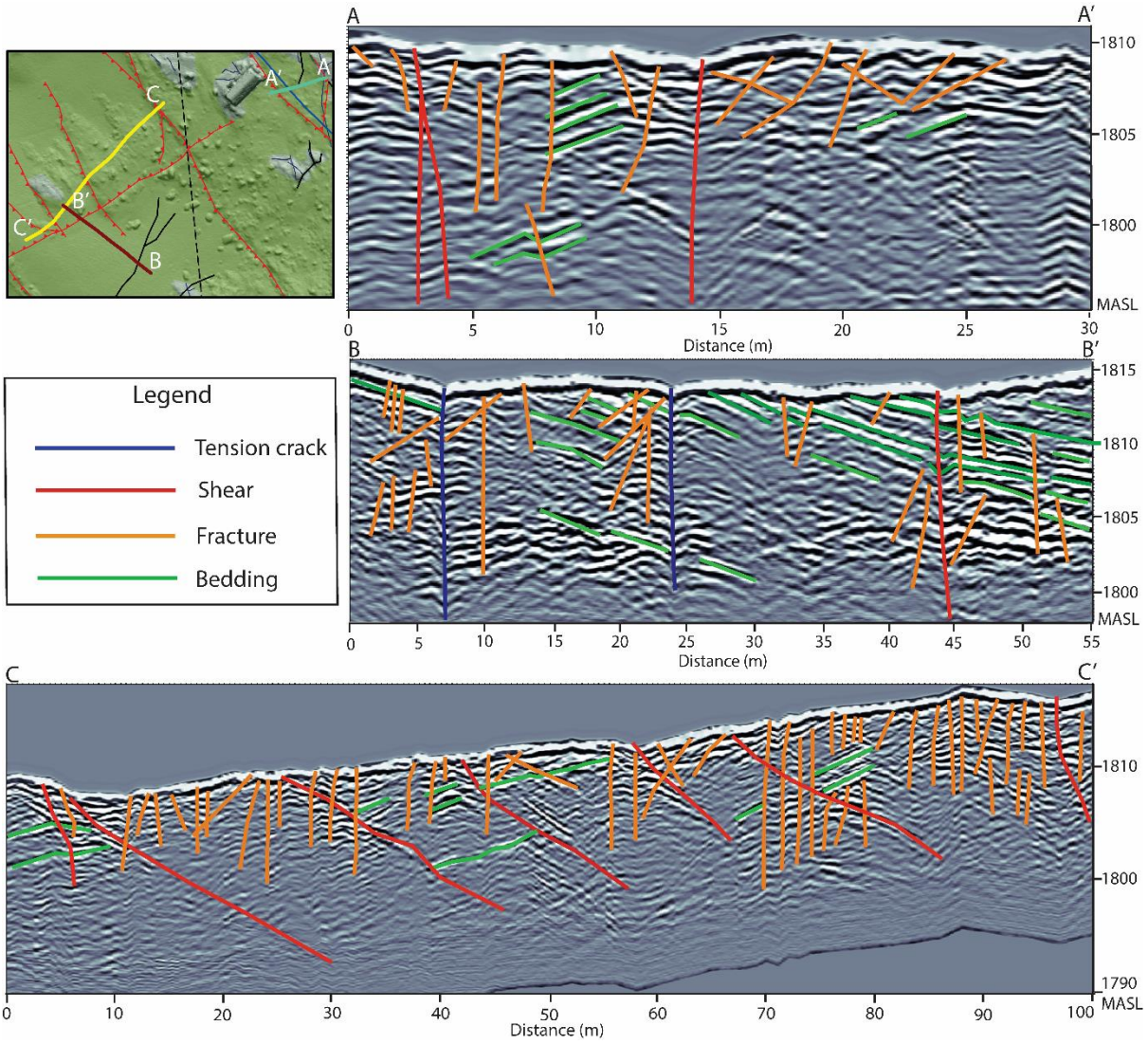

Figure 10. GPR transects from the Mueller Hut area. A-A') Transect 1 going NE-SW approximately 20 m from Mueller Hut. The two shear features identified in the left of the image are considered to be the eastern most scarps for the rockslide retrogressive zone. B-B') Transect 2 going E-W through the northern limit of a large tension crack. C-C') Transect 3 going N-W through several large shear features directly south of Mueller Hut.

Slope Stability Modelling

The calculated critical SRF for the isotropic model was greater than the one obtained for the anisotropic model. More importantly, the displacement pattern at the critical SRF model is on the east side of Mueller Ridge for the isotropic model whereas it shifts to the western (i.e. Mueller Rockslide) side when the bedding anisotropy is considered (Fig. 11). This numerical modelling assessment provides simple but useful support for the idea that the Mueller Rockslide is structurally-influenced by the bedding. However, neither model produced a SRF approaching a critical value of 1, suggesting that the rock strength parameters used or the

bedding orientation were inappropriate (i.e. too strong), or groundwater or other processes not included are important for bringing the slope to a critically-stable state. Additional models considering a wider range of strength parameters, the influence of more subtle structural weaknesses (e.g. discontinuity sets) and potential triggers (groundwater and seismicity), will be investigated in the future.

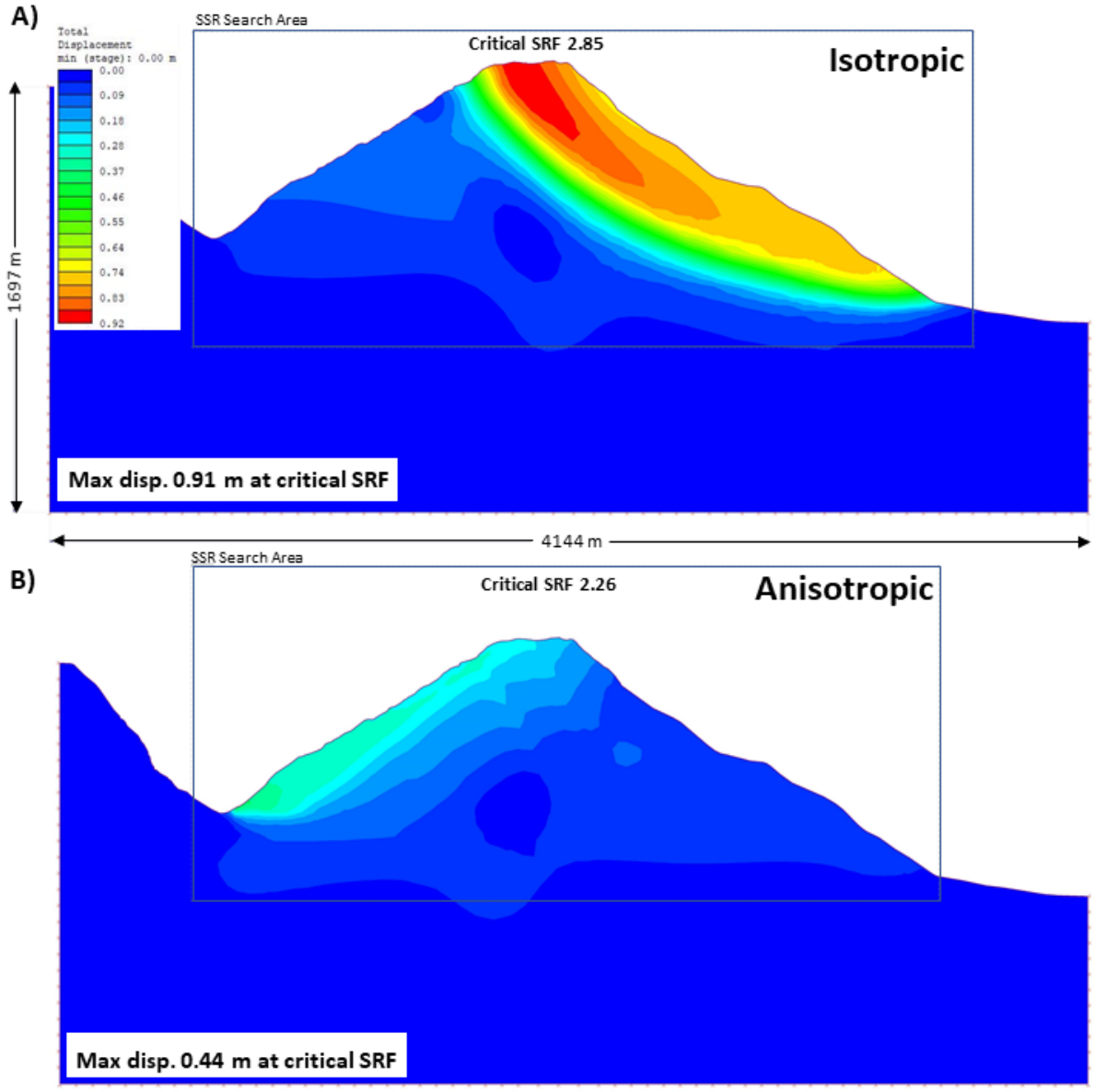

Figure 11. Total displacement magnitude across Mueller Ridge at the critical strength reduction factor for an A) isotropic and B) anisotropic models. Location of the cross-section is equivalent to the one shown in Figure 2.

676 **Discussion**

677 **Comparisons between SRT, GPR and geomorphic mapping.**

678 Geophysical surveys including SRT and GPR, have become common place in recent decades
679 for quantifying rock mass qualities and discontinuities of rock slope failures (Heincke et al.
680 2010; Bekler et al. 2011; Meric et al. 2005). SRT and GPR have been previously combined in
681 rock cavity identification or in the study of smaller fracture zones (De Giorgi and Leucci 2014;
682 Heincke et al, 2006). Herein, we further demonstrate the utility of these two techniques for
683 confirming the presence and subsurface continuity of deformation indicated at the surface by
684 scarps, and for supporting geotechnical mapping of fractures into the subsurface, especially
685 where bedrock is obscured by debris. In addition, we show how SRT can be used to reveal
686 changes in fracture density at depth, as well as revealing the thickness of surficial materials
687 overlying bedrock.

688 This study has shown a strong relationship between areas of increased fracturing (high fracture
689 percentage) in the SRT with fractures identified within the GPR. Areas of low P-wave velocity
690 (<2.0 kms-1) and high fracture percentage (>30%) often were located in areas with numerous
691 fractures. In particular, several shear surfaces were distinguishable within the SRT in the Old
692 Hut and Mueller Hut transects, consistent with field mapping (scarp identification) and GPR.
693 For the Mueller Hut transect, ray density analysis showed this particularly well as the transect
694 passed through a more intact bedrock zone, allowing for the difference between intact and
695 highly fractured bedrock to be seen.

696 Inclusion of the GPR also allowed for the identification of bedding planes which were not
697 readily apparent from the SRT data; this information was useful for identifying shear surfaces
698 at depth and linking them to mapped scarps at the surface. While the GPR was also useful for
699 detecting discontinuities, GPR is not effective at imaging feature parallel to the radar transect
700 (i.e. vertical features along the transect). We believe tension cracks and other vertical
701 discontinuities within the GPR data are underrepresented. Combining the two methods (SRT
702 and GPR) helps to minimise some of the shortcomings of the individual techniques and
703 provided richer results. This enabled a more comprehensive assessment of all structural
704 features throughout the surveyed area and the methods complimented each other to provide a
705 view of broader rock mass quality and the relationship to bedding, fractures and shear planes.
706 Overall, the three techniques (GPR, SRT and field mapping) were consistent and complimented
707 each and here they have confirmed the presence of major open fractures, and vertical
708 deformation along features consistent at the top of the rockslope. The kinematic analysis
709 suggests that planar failure along bedding is unlikely here, and instead the geophysics indicates

that this deformation is being accommodated by sub-vertical joints, likely the same ones controlling the headscarps. This suggests that the rock mass of the upper part of the rockslope is facilitating retrogressive enlargement of the rockslide.

Access and safety made it unfeasible to extend the geophysical surveys across the entire rockslide, and the depth of penetration by SRT was limited by use of mechanical means of seismic signal generation (i.e. sledge hammer). Nonetheless, this study demonstrates the utility of these techniques on large rock slope failures and DSGSDs, if they can be safely deployed and especially if larger seismic sources can be generated (e.g. dynamite).

Structural controls on rockslide morphology

Geomorphic mapping, SRT and GPR have identified an extensive fracture network at the Sealy Range. The discontinuity sets in Figs. 5 and 6 are equivalent with fractures commonly associated with folding (Price and Cosgrove 1990). Specifically, discontinuity sets closely align with fractures oriented parallel, perpendicular and orthogonal to an anticline (Fig. 12). Excluding bedding, discontinuity sets identified along the ridgeline align parallel (R2, R6) and perpendicular (R3, R4) to the main anticline hingeline (Fig. 5; Fig. 12) and are classed as extensional joint sets. R5 and R7 are orthogonal fractures in the retrogressive zone and are classified as shear fractures. Discontinuity sets within the landslide zone are predominantly orthogonal to the main hingeline and dip to the northwest (L2), southeast (L5) and southwest (L3) and are interpreted as shear fractures.

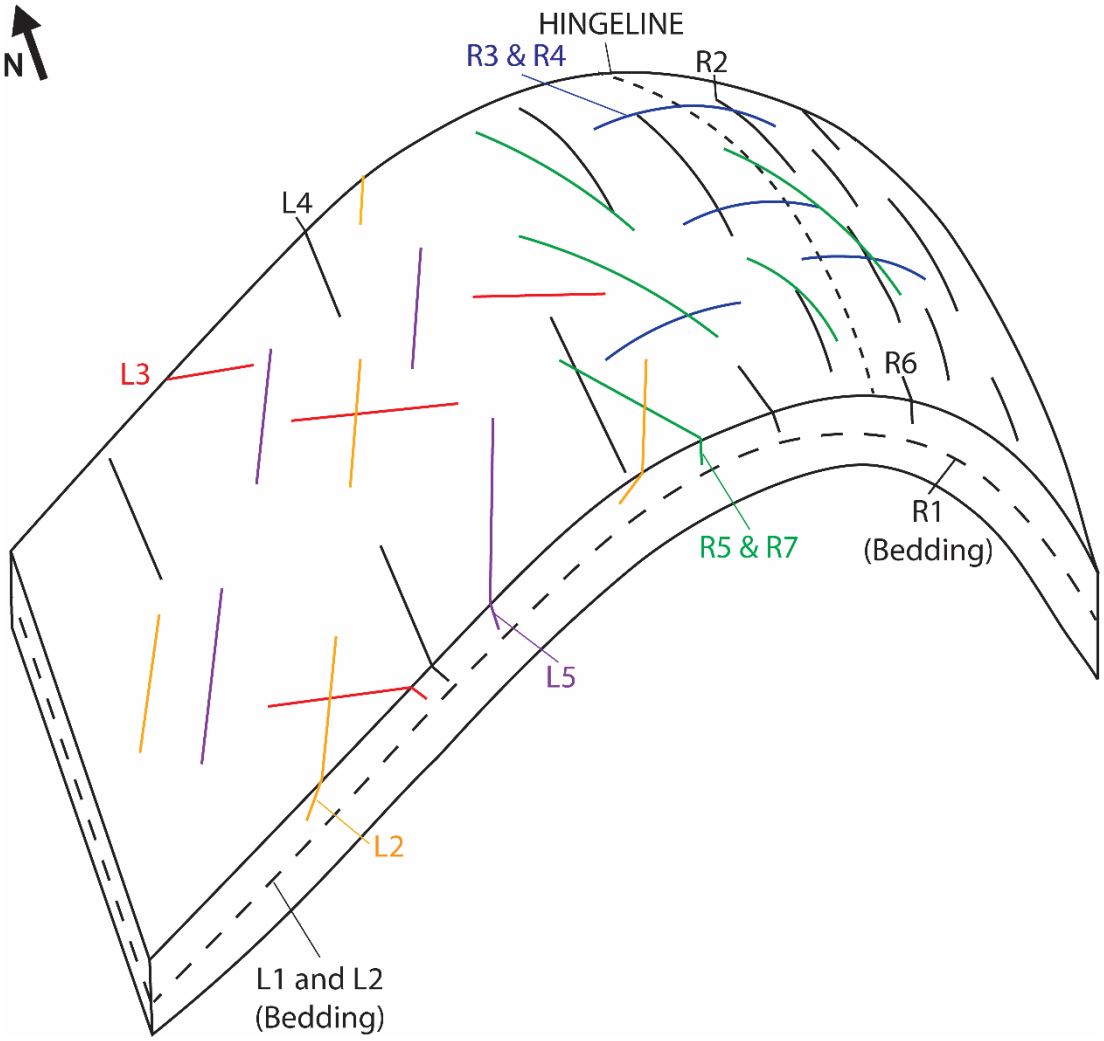

Figure 12. Primary discontinuity sets seen within the Sealy Range and northward plunging Kitchener Anticline. Adapted from Price and Cosgrove 1990.

Preconditioning and morphology of the Mueller Rockslide has been strongly controlled by its location on the dip slope of the Kitchener Anticline. In fact, without structural controls and anisotropy, failure of the hillslope would only occur to the east as indicated by modelling (Fig. 11. Headscarp morphology has strongly aligned with the L3 and L4 fractures (Fig. 12) in a northwest – southeast direction with the steep dips of the fractures accounting for the occurrence of block toppling in this area. These joint sets also align with the newly mapped scarps developing along the ridgeline (R5 and R7; Fig. 12) which appear to be facilitating downslope movement of the upper ridge. They appear to act as rear-release structures, similar to what has been previously observed by Brideau et al (2009) at the Hope slide in British Columbia and the Randa Rockslide in Switzerland. Continued block toppling and rockslide movement has steepened this headscarp zone, allowing for the potential for daylighting of several joint sets and the increased potential for wedge failure and block toppling as indicated in the kinematic analysis (Fig. 6). The north – south oriented R2 and R6 joint sets may also be

748 acting as a minor rear-release mechanism, resulting in the formation of large tension cracks
749 above the headscarp. Lateral release structures are also essential for allowing the rockslide to
750 develop (Brideau et al, 2009) Several east-west oriented releasing scarps were identified (R3
751 and R4; Fig. 12) particularly to the north-west of Mueller Hut and to the south-west of Mueller
752 Hut above the arcuate headscarp (Fig. 4). The importance of these rear and lateral release
753 structures is highlighted by Brideau and Stead (2012) who demonstrate that persistence of these
754 release surfaces along with their orientation relative to the slope dip direction are essential for
755 controlling rockslide failure initiation as well as rockslide morphology.
756 The inability to investigate the deep subsurface of the rockslide body has meant that little is
757 directly known about the rockslide failure surface. Instead we make assumptions on the failure
758 surface based on scarp and shear surface morphology resolved from the ridgeline seismic
759 transects, observations of rock type and rock mass quality, and discontinuity mapping. The
760 failure surface is assumed to be along bedding (weak argillite layers), consistent with GPS
761 survey data shows that movement in a down-dip direction (285°) rather than a downslope
762 direction (270°) in the central rockslide (McColl 2012b), and supported by the stability
763 modelling (Fig. 11). However, kinematic analysis indicates simple planar failure marginal or
764 oblique to the slope direction as only one bedding measurement fell inside the failure window
765 (Fig. 6, 7), consistent with the observation that measured dip of bedding is steeper than the
766 slope of the rockslide. While this makes daylighting of a failure surface along bedding unlikely,
767 there is very little known of the orientation and condition of bedding at the toe of the slope. It
768 is feasible for bedding to fold back into a different structure (e.g. syncline) at the toe and we
769 observe bedrock on the opposite side of the valley appears lithologically and structurally
770 different. Consequently, bedding may curve into the slope face at the toe of Mueller Rockslide,
771 facilitating kinematic release and sliding along bedding into the valley (Fig. 13a). Alternatively,
772 movement may be accommodated at the toe by ductile deformation (buckling; Fig. 13b) or
773 release along one or more fractures (Fig. 13c).
774

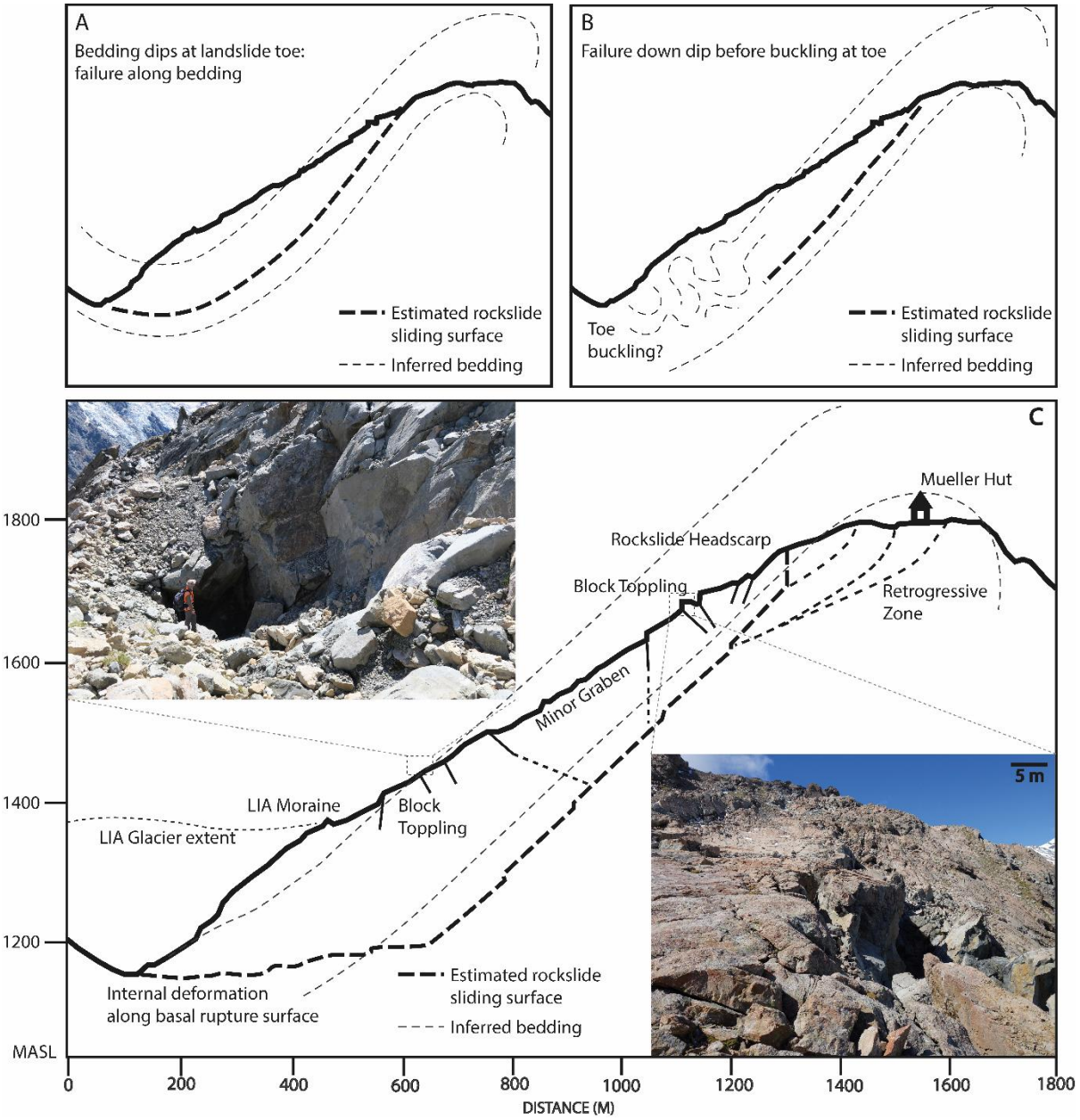

Figure 13. Cross section and models of the Mueller Rockslide. A) Bedding inferred to dip into valley allowing for kinematic release and failure along bedding. B) Failure along bedding and movement accommodation by ductile deformation and toe buckling at base of slope. C) Stepped failure approximately down dip with deformation at toe accommodated by release along fractures. Top image shows block toppling in the in the lower rockslide (looking north). Bottom image shows the main headscarp and blocking toppling (looking south). Given the height of the headscarps (30 m), plus the identification of a zone of retrogressive development extending 150-200 m east of the headscarp, we assume rockslide thickness to be several tens of metres deep near the top of the rockslide. An increasing thickness downslope is inferred from the observation that bedding dips at a steeper angle than the rockslide slope.

While toe buckling by ductile processes occurs in the Southern Alps within the highly anisotropic schist, this process is less likely to occur in the high strength brittle greywacke. Finite element modelling with the assumed bedding orientation suggests a low failure potential

with a high SRF of 2.26 for the western rockslope with displacement of only 0.44 m at that SRF. We therefore suggest that if bedding orientation does not permit kinematic admissibility, breakout along fractures that step across bedding is a more likely scenario. We observe fractures stepping and shearing across bedding at the top of the slope. GPR and SRT (Mueller Hut transect) show shearing across bedding, facilitated by the joint sets in the retrogressive zone, and at the top of the headscarp where the identified scarp dips near vertically through bedding. Stepping across bedding may in fact be a characteristic feature of the whole failure surface, creating a stepped failure surface connecting planes of weakness (i.e. bedding). Stepped sliding planes have been identified in other large rockslope failures (Oppikofer et al. 2011; Sturzenegger and Stead 2012; Tannant et al. 2017). Ultimately, failure of the rockslope may be accommodated by a combination of geological structure (bedding) and rock mass conditions (joints), both of which are influenced by the Kitchener Anticline.

While the Mueller Rockslide has previously been described as a DSGSD (McColl and Davies 2013), observations from field work and geophysical surveys indicate the slope failure does not display many of the normal attributes seen in DSGSDs. Only a single uphill facing scarp (on the landslide body) was identified, which are normally typical of DSGSDs. Instead, we see a discontinuous but clear set of normal scarps defining the crown. As well, while a bedding failure surface has not been confirmed, movement direction down-dip indicates failure along bedding is feasible. Therefore, we propose that the Mueller Rockslide can be better described as a rock compound slide. As defined by Hungr et al. (2014), rock compound slides are those which form along several planes or a disconnected sliding surface and must undergo some internal deformation to allow movement. Continued internal deformation and weakening of the rock mass (in our case mostly at the toe) may eventually lead to rapid failure. Rock compound slides often have a steep main scarp that cuts through the rock mass (in our case across bedding and along joint sets), and connects to the failure surface.

In summary, structural controls such as bedding and rock mass properties (i.e. joint sets) likely influence the failure mechanism and together explain the rockslide morphology, observed deformation of the rock mass, and why the slope has not yet failed catastrophically. Future work will include stability modelling to test these ideas and explore further the relationship between the observed morphological structures, movement of the slope, and the geological controls.

824 **Rockslide development towards rapid failure**

825 Slow moving rockslope instabilities can transition to rapid and catastrophic failures (Pánek et
826 al. 2011c; Kilburn and Petley 2003; Geertsema et al. 2006). While assessing the temporal
827 evolution of the Mueller Rockslide has not been the focus of this research, the data collected
828 here can allow a qualitative assessment of whether the Mueller Rockslide could accelerate and
829 fail rapidly, either overtime as a progressive failure or through an external trigger like strong
830 earthquake shaking.

831 The evolution of large rockslides towards rapid failure is an important avenue of landslide
832 hazard research (Hungr 2007). Several studies (e.g. Glastonbury and Fell 2008a, 2008b, 2010;
833 Eberhardt et al. 2004; Crosta and Agliardi 20030) have attempted to identify key structural and
834 geomechanical properties commonly found in rockslides which transition to catastrophic
835 failure and found several common factors, which can indicate potential for catastrophic failure.
836 Common characteristics include a high strength rock mass that facilitates failure en masse
837 rather than smaller slope failures from highly disaggregated rock masses, loss of toe buttressing
838 support, and strongly defined lateral margins (particularly important for deep rockslides) which
839 lie normal to anisotropy (Glastonbury and Fell 2010, 2008b). As well, first time failure as
840 opposed to those experiencing reactivation are more likely to progress to rapid failure. In
841 contrast, slow moving landslides, which do not progress to rapid failure more often occur in
842 weak, disaggregated rock masses and in slopes where the basal rupture surface angle is less
843 than the residual friction angle (Glastonbury and Fell 2008a).

844 Our observations show that the Mueller Rockslide has some characteristics in favour of
845 catastrophic failure and others against. GSI values from rock mass characterisation of 50-60
846 for sandstone and 30-40 for argillite are low to fair, possibly suggesting disintegration rather
847 than failure en masse. However, while the rockslide is clearly fractured, it occupies the entire
848 slope from toe to ridge crest and extends for about 1 km along the ridge, suggesting it is failing
849 as a large mass. The slope has clearly been debuttressed, as a result of thinning of the Mueller
850 Glacier, but has likely undergone erosion by the glacier too, explaining the steepened section
851 of hillslope below the break in slope of the LIA moraine limit (Fig. 13). Lateral restraints are
852 identified within the kinematic analysis (R3 and R4 discontinuity sets) and lie normal to
853 anisotropy (perpendicular to bedding) which is characteristic of potential rapid failure. While
854 the Mueller Rockslide is currently unstable (indicated by movement data; McColl, 2012b) it is
855 probably not a first time failure i.e. sliding surface is at residual strength as the rockslide may
856 have been moving for decades to centuries. Displaced lateral moraine shows movement has
857 been ongoing for a significant period of time without yet accelerating to catastrophic failure.

858 This magnitude of displacement, however, suggests that the friction angle of the rupture surface
859 is likely to be at residual values (<33°), and this is considerably less than the dip of the bedding
860 assumed to be the sliding surface (which is a characteristic of rapid failure). Putting some of
861 these conditions together and following the decision tree of Glastonbury and Fell (2008a) for
862 an internally sheared, compound slide, the probability of very rapid to extremely rapid velocity
863 for the Mueller Rockslide is between 55-65%. The upper value represents the case of a rapid
864 external load (e.g. a strong earthquake). Under this decision tree scenario, we assume that the
865 failure surface is at residual strength (i.e. a through-going, well-developed failure surface
866 extending to the toe); if not at residual strength yet, the probabilities increase to 80-90%. The
867 gradual development of a through-going failure surface at the toe, by connection of fractures
868 and breakage of rock bridges, may represent progressive failure of this slope; this could allow
869 the transition to catastrophic acceleration.
870 These results appear to contradict the simplified modelling results presented in Figure 11 which
871 indicates failure to be unlikely. However, this model does not account for the influence of toe
872 debuttressing, seismicity and ground water fluctuations. While failure along bedding is
873 feasible, our results indicate it will not occur without external forcing, or through progressive
874 loss of strength. Similar results have been seen within the Moosfluh Landslide and other
875 rockslope instabilities surrounding the Aletsch Glacier. Gramiger et al. 2017 and Glueer et al.
876 2019 show incremental damage associated with repeat glacier cycles play a significant role in
877 gradually weakening rock masses. In addition, while glacier debuttressing has been identified
878 as a preparatory factor for many alpine rock slope failures, in the latter stages of retreat glacier
879 ice can induce viscous flow in unstable rock slopes through deformation (McColl and Davies
880 2013).
881 Future investigations on kinematics and movement history may provide insights on the
882 relationship between movement and environmental drivers (e.g. pore-water pressure) and
883 external forcings (e.g. seismic shaking). Additional modelling is required to assist in the
884 determination of rockslide failure potential.
885
886 **Conclusions**
887 This paper summarises a combination of field mapping, fracture mapping, kinematic analysis
888 and geophysical methods to present the structural controls and preconditioning factors of
889 Mueller Rockslide. An extensive fracture network throughout the Sealy Range in proximity to
890 the rockslide as well as several scarps above the main rockslide headscarp were newly
891 identified. SRT and GPR have been successfully combined and show extensive fracturing to at

least 10 m depth as well as the presence of several shear planes that coincide with mapped scarps at the surface. Several large tension cracks have also been identified above the main rockslide headscarp. The identification of several scarps and tension cracks indicates retrogressive development of the rockslide into the ridgetop.

Kinematic analysis was performed for discontinuities within the rockslide and ridgeline areas. There is a low feasibility for planar sliding and an increased feasibility for wedge and toppling failure was identified through the headscarp and ridgetop. Although there is a limited feasibility for planar sliding, the movement direction of the rockslide is down-dip (285°) as opposed to down-slope (270°), suggesting an influence of bedding, further supported by our stability modelling. We therefore estimate the rockslide is moving along a stepped, discontinuous sliding surface along and through the interbedded argillite and sandstone.

This research shows the formation of the Mueller Rockslide has been strongly influenced by the folding of Kitchener Anticline with failure controlled by bedding angle and orientation and the presence of joint sets commonly associated with anticline formation. While slow moving, the Mueller Rockslide exhibits some features commonly identified within rockslopes that transition to rapid, catastrophic landslides. A strong and predominantly intact rock mass as well as the presence of strongly defined lateral release structures increase the potential for rapid failure.

Future work should focus on identifying key triggers for rockslide movement and investigate the development of the rockslide through monitoring, modelling and cosmogenic dating. The investigation of potential seismic and hydrological triggers should also be completed given the high seismicity, rainfall and snow melt levels that affect the site.

References

Agliardi, F., Crosta, G. and Zanchi, A., 2001. Structural constraints on deep-seated slope deformation kinematics. Engineering Geology, 59(1-2), 83-102.

Agliardi, F., Crosta, G.B., Zanchi, A. and Ravazzi, C., 2009a. Onset and timing of deep-seated gravitational slope deformations in the eastern Alps, Italy. Geomorphology, 103(1), 113-129.

Agliardi, F., Zanchi, A. and Crosta, G.B., 2009b. Tectonic vs. gravitational morphostructures in the central Eastern Alps (Italy): constraints on the recent evolution of the mountain range. Tectonophysics, 474(1-2), 250-270.

Ambrosi, C. and Crosta, G.B., 2011. Valley shape influence on deformation mechanisms of rock slopes. Geological Society, London, Special Publications, 351(1), 215-233.

926 Archibald, G.C., Carey J.M., Ries. W.F., McColl. S.T., 2016. Geological inspection and baseline
927 monitoring of Mueller Hut, Aoraki/ Mt Cook National Park. GNS Science Consultancy Report
928 2016/80 June 2016.
929 Aringoli, D., Farabollini, P., Giacopetti, M., Materazzi, M., Paggi, S., Pambianchi, G., Pierantoni, P.P.,
930 Pistolesi, E., Pitts, A. and Tondi, E., 2016. The August 24th 2016 Accumoli earthquake: Surface
931 faulting and deep-seated gravitational slope deformation (DSGSD) in the Monte Vettore
932 area. Annals of Geophysics, 59.
933 Ballantyne, C. K., Sandeman, G. F., Stone, J. O., Wilson, P., 2014a. Rock-slope failure following Late
934 Pleistocene deglaciation on tectonically stable mountainous terrain. Quaternary Science Reviews,
935 86, 144-157.
936 Ballantyne, C. K., Stone, J. O., 2009. Rock-slope failure at Baosbheinn, Wester Ross, NW Scotland:
937 age and interpretation. Scottish Journal of Geology, 45 (2), 177-181.
938 Ballantyne, C. K., Wilson, P., Gheorghiu, D., Rodés, À., 2014b. Enhanced rock-slope failure following
939 ice-sheet deglaciation: timing and causes. Earth Surface Processes and Landforms, 39 (7), 900-913.
940 Ballantyne, C.K., 2002. Paraglacial geomorphology. Quaternary Science Reviews, 21 (18-19), 1935-
941 2017.
942 Ballantyne, C.K., Stone, J.O., 2013. Timing and periodicity of paraglacial rock-slope failures in the
943 Scottish Highlands. Geomorphology, 186, 150-161.
944 Barbarano, M., Agliardi, F., Crosta, G.B. and Zanchi, A., 2015. Inherited and active tectonic controls
945 on the Piz Dora DSGSD (Val Müstair, Switzerland). In Engineering Geology for Society and
946 Territory-Volume 2 (pp. 605-608). Springer, Cham.
947 Beck, A.C., 1968. Gravity faulting as a mechanism of topographic adjustment. New Zealand journal of
948 geology and geophysics, 11(1), 191-199.
949 Bekler, T., Ekinci, Y.L., Demirci, A., Erginal, A.E. and Ertekin, C., 2011. Characterization of a
950 landslide using seismic refraction, electrical resistivity and hydrometer methods, Adatepe–
951 Çanakkale, NW Turkey. Journal of Environmental and Engineering Geophysics, 16(3), 115-126.
952 Bovis, M.J. and Evans, S.G., 1996. Extensive deformations of rock slopes in southern Coast Mountains,
953 southwest British Columbia, Canada. Engineering Geology, 44(1-4), 63-182.
954 Bovis, M.J., 1982. Uphill-facing (antislope) scarps in the Coast Mountains, southwest British
955 Columbia. Geological Society of America Bulletin, 93(8), 804-812.
956 Brideau, M.A. and Stead, D., 2012. Evaluating kinematic controls on planar translational slope failure
957 mechanisms using three-dimensional distinct element modelling. Geotechnical and Geological
958 Engineering, 30(4), 991-1011.
959 Brideau, M.A., Yan, M. and Stead, D., 2009. The role of tectonic damage and brittle rock fracture in
960 the development of large rock slope failures. Geomorphology, 103(1), 30-49.
961 Chigira, M. and Kiho, K., 1994. Deep-seated rockslide-avalanches preceded by mass rock creep of
962 sedimentary rocks in the Akaishi Mountains, central Japan. Engineering Geology, 38(3-4), 221-230.

963 Clarke, B.A., Burbank, D.W., 2011. Quantifying bedrock-fracture patterns within the shallow
964 subsurface: Implications for rock mass strength, bedrock landslides, and erodibility. Journal of
965 Geophysical Research: Earth Surface, 116 (F4).
966 Clayton, A., Stead, D., Kinakin, D. and Wolter, A., 2017. Engineering geomorphological interpretation
967 of the Mitchell Creek Landslide, British Columbia, Canada. Landslides, 14(5), 1655-1675.
968 Cook GK. 2001. Rock mass structure and intact rock strength of New Zealand greywackes. M.Sc. thesis,
969 University of Canterbury.
970 Coquin, J., Mercier, D., Bourgeois, O., Cossart, E. and Decaulne, A., 2015. Gravitational spreading of
971 mountain ridges coeval with Late Weichselian deglaciation: impact on glacial landscapes in
972 Tröllaskagi, northern Iceland. Quaternary Science Reviews, 107, 197-213.
973 Cossart, E., Braucher, R., Fort, M., Bourlès, D. L., Carcaillet, J., 2008. Slope instability in relation to
974 glacial debuttressing in alpine areas (Upper Durance catchment, southeastern France): Evidence
975 from field data and 10Be cosmic ray exposure ages. Geomorphology, 95(1-2), 3-26.
976 Cox, S.C., Barrell, D.J.A., 2007. Geology of the Aoraki area. Institute of Geological and Nuclear
977 Sciences 1:250000 Geological map. Lower Hutt, New Zealand: GNS Science.
978 Crosta, G.B. and Agliardi, F., 2003. Failure forecast for large rock slides by surface displacement
979 measurements. Canadian Geotechnical Journal, 40(1), 176-191.
980 Crosta, G.B., Di Prisco, C., Frattini, P., Frigerio, G., Castellanza, R. and Agliardi, F., 2014. Chasing a
981 complete understanding of the triggering mechanisms of a large rapidly evolving
982 rockslide. Landslides, 11(5), 747-764.
983 Crosta, G.B., Frattini, P. and Agliardi, F., 2013. Deep seated gravitational slope deformations in the
984 European Alps. Tectonophysics, 605, 13-33.
985 Crozier, M.J., Deimel, M.S. and Simon, J.S., 1995. Investigation of earthquake triggering for deep-
986 seated landslides, Taranaki, New Zealand. Quaternary International, 25, 65-73.
987 De Giorgi, L. and Leucci, G., 2014. Detection of hazardous cavities below a road using combined
988 geophysical methods. Surveys in Geophysics, 35(4), 1003-1021.
989 Draebing, D., Krautblatter, M., 2012. P-wave velocity changes in freezing hard low-porosity rocks: a
990 laboratory-based time-average model. The Cryosphere, 6, 1163-1174.
991 Dramis, F. and Sorriso-Valvo, M., 1994. Deep-seated gravitational slope deformations, related
992 landslides and tectonics. Engineering Geology, 38(3-4), 231-243.
993 Eberhardt, E., Stead, D. and Coggan, J.S., 2004. Numerical analysis of initiation and progressive failure
994 in natural rock slopes—the 1991 Randa rockslide. International Journal of Rock Mechanics and
995 Mining Sciences, 41(1), 69-87.
996 El Bedoui, S., Guglielmi, Y., Lebourg, T. and Pérez, J.L., 2009. Deep-seated failure propagation in a
997 fractured rock slope over 10,000 years: The La Clapière slope, the south-eastern French
998 Alps. Geomorphology, 105(3-4), 232-238.

999 Fey, C., Wichmann, V. and Zangerl, C., 2017. Reconstructing the evolution of a deep seated rockslide
1000 (Marzell) and its response to glacial retreat based on historic and remote sensing
1001 data. Geomorphology, 298, 72-85.
1002 Ganerød, G.V., Grøneng, G., Rønning, J.S., Dalsegg, E., Elvebakk, H., Tønnesen, J.F., Kveldsvik, V.,
1003 Eiken, T., Blikra, L.H., Braathen, A., 2008. Geological model of the Åknes rockslide, western
1004 Norway. Engineering Geology, 102(1), 1-18.
1005 Geertsema, M., Clague, J.J., Schwab, J.W. and Evans, S.G., 2006. An overview of recent large
1006 catastrophic landslides in northern British Columbia, Canada. Engineering Geology, 83 (1-3), 120-
1007 143.
1008 Gellatly, A.F., 1985. Historical records of glacier fluctuations in Mt Cook National Park, New Zealand:
1009 a century of change. Geographical journal, 151(1), 86-99.
1010 Ghirotti, M., Martin, S. and Genevois, R., 2011. The Celentino deep-seated gravitational slope
1011 deformation (DSGSD): structural and geomechanical analyses (Peio Valley, NE Italy). Geological
1012 Society, London, Special Publications, 351(1), 235-251.
1013 Glastonbury, J. and Fell, R., 2008a. Geotechnical characteristics of large slow, very slow, and extremely
1014 slow landslides. Canadian Geotechnical Journal, 45(7), 984-1005.
1015 Glastonbury, J. and Fell, R., 2008b. A decision analysis framework for the assessment of likely post-
1016 failure velocity of translational and compound natural rock slope landslides. Canadian Geotechnical
1017 Journal, 45(3), 329-350.
1018 Glastonbury, J. and Fell, R., 2010. Geotechnical characteristics of large rapid rock slides. Canadian
1019 Geotechnical Journal, 47(1), 116-132.
1020 Glueer, F., Loew, S. and Manconi, A., 2019. Paraglacial history and structure of the Moosfluh
1021 Landslide. Geomorphology.
1022 Gori, S., Falcucci, E., Dramis, F., Galadini, F., Galli, P., Giaccio, B., Messina, P., Pizzi, A., Sposato,
1023 A. and Cosentino, D., 2014. Deep-seated gravitational slope deformation, large-scale rock failure,
1024 and active normal faulting along Mt. Morrone (Sulmona basin, Central Italy): Geomorphological
1025 and paleoseismological analyses. Geomorphology, 208, 88-101
1026 Grämiger, L.M., Moore, J.R., Gischig, V.S. and Loew, S., 2018. Thermomechanical stresses drive
1027 damage of Alpine valley rock walls during repeat glacial cycles. Journal of Geophysical Research:
1028 Earth Surface, 123(10), 2620-2646.
1029 Grämiger, L.M., Moore, J.R., Gischig, V.S., Ivy-Ochs, S. and Loew, S., 2017. Beyond debuttressing:
1030 Mechanics of paraglacial rock slope damage during repeat glacial cycles. Journal of Geophysical
1031 Research: Earth Surface, 122 (4), 1004-1036.
1032 Hancox, G. T., 1994. Report on Mt Cook National Park hut site inspections and establishment of
1033 monitoring lines, April 1994. Institute of Geological and Nuclear Sciences, Client Report 353902.20,
1034 prepared for Department of Conservation, Mt Cook National Park; 32.

Hancox, G.T., 1998. Pilot study for Baseline Geological Inspection of DOC Backcountry Huts: Inspections of alpine hut sites in the Mt Cook and Westland National Parks, March 1998. Institute of Geological and Nuclear Sciences Client Report 43713B.

Hauck, C., Vonder Mühll, D., 2003. Evaluation of geophysical techniques for application in mountain permafrost studies. Zeitschrift für Geomorphologie, Supplement, 132, 161-190.

Havenith, H.B., Jongmans, D., Abdrakhmatov, K., Trefois, P., Delvaux, D., Torgoev, I.A., 2000. Geophysical Investigations of Seismically Induced Surface Effects: Case Study Of A Landslide In The Suusamyr Valley, Kyrgyzstan. Surveys in Geophysics, 21(4), 351-370.

Havenith, H.B., Jongmans, D., Faccioli, E., Abdrakhmatov, K., Bard, P.Y., 2002. Site Effect Analysis around the Seismically Induced Ananevo Rockslide, Kyrgyzstan. Bulletin of the Seismological Society of America, 92(8), 3190-3209.

Heincke, B., Günther, T., Dalsegg, E., Rønning, J.S., Ganerød, G.V., Elvebakk, H., 2010. Combined three-dimensional electric and seismic tomography study on the Åknes rockslide in western Norway. Journal of Applied Geophysics, 70(4), 292-306.

Heincke, B., Maurer, H., Green, A.G., Willenberg, H., Spillmann, T., Burlini, L., 2006. Characterizing an unstable mountain slope using shallow 2D and 3D seismic tomography. Geophysics, 71(6), 241-256.

Hewitt, K., Clague, J.J. and Orwin, J.F., 2008. Legacies of catastrophic rock slope failures in mountain landscapes. Earth-Science Reviews, 87(1-2), 1-38.

Hou, Y., Chigira, M. and Tsou, C.Y., 2014. Numerical study on deep-seated gravitational slope deformation in a shale-dominated dip slope due to river incision. Engineering geology, 179, 59-75.

Hungr, O., 2007. Dynamics of rapid landslides. In Progress in landslide science (pp. 47-57). Springer, Berlin, Heidelberg.

Hungr, O., Leroueil, S. and Picarelli, L., 2014. The Varnes classification of landslide types, an update. Landslides, 11(2), 167-194.

Jaboyedoff, M., Penna, I., Pedrazzini, A., Baroň, I. and Crosta, G.B., 2013. An introductory review on gravitational-deformation induced structures, fabrics and modeling. Tectonophysics, 605, 1-12.

James, M.R., Robson, S., 2014. Mitigating systematic error in topographic models derived from UAV and ground-based image networks. Earth Surface Processes and Landforms, 39(10), 1413-1420.

Kilburn, C.R. and Petley, D.N., 2003. Forecasting giant, catastrophic slope collapse: lessons from Vajont, Northern Italy. Geomorphology, 54(1-2), 21-32.

Kirkbride, M.P. and Warren, C.R., 1999. Tasman Glacier, New Zealand: 20th-century thinning and predicted calving retreat. Global and Planetary Change, 22 (1-4), 11-28.

Kliche, C.A., 1999. Rock slope stability. SME. Littleton, Co.

Kos, A., Amann, F., Strozzi, T., Delaloye, R., Ruette, J. and Springman, S., 2016. Contemporary glacier retreat triggers a rapid landslide response, Great Aletsch Glacier, Switzerland. Geophysical Research Letters, 43 (24), 466-474.

Krautblatter, M., Draebing, D., 2014. Pseudo 3D - P-wave refraction seismic monitoring of permafrost in steep unstable bedrock. Journal of Geophysical Research: Earth Surface, 119(2), 287-299.

Lillie, A.R. and Gunn, B.M., 1964. Steeply plunging folds in the sealy range, southern Alps. New Zealand journal of geology and geophysics, 7 (3), 403-423.

Mahr, T., 1977. Deep—Reaching gravitational deformations of high mountain slopes. Bulletin of the International Association of Engineering Geology-Bulletin de l'Association Internationale de Géologie de l'Ingénieur, 16(1), 121-127.

Marinos, V, Marinos, P. and Hoek, E., 2005. The geological strength index: applications and limitations. Bulletin of Engineering Geology and the Environment, 64(1), 55-65.

Martinotti, G., Giordan, D., Giardino, M. and Ratto, S., 2011. Controlling factors for deep-seated gravitational slope deformation (DSGSD) in the Aosta Valley (NW Alps, Italy). Geological Society, London, Special Publications, 351(1), 113-131.

Matsui T, San K-C. 1992. Finite element slope stability analysis by shear strength reduction technique. Soils and Foundations 32: 59-70.

McColl, S. T., Davies, T. H. R., 2013. Large ice-contact slope movements: glacial buttressing, deformation and erosion. Earth Surface Processes and Landforms, 38 (10), 1102-1115.

McColl, S.T., 2012a. Paraglacial rock-slope stability. Geomorphology, 153, 1-16.

McColl, S.T., 2012b. Paraglacial Rockslope Stability. Phd Thesis, University of Canterbury.

McColl, S.T., Draebing, D., 2019. Rock slope instability in the proglacial zone: State of the Art. In: T. Heckmann, D. Morche (Eds.), Geomorphology of proglacial systems - Landform and sediment dynamics in recently deglaciated alpine landscapes, 119-141.

Meric, O., Garambois, S., Jongmans, D., Wathelet, M., Chatelain, J.L., Vengeon, J.M., 2005. Application of geophysical methods for the investigation of the large gravitational mass movement of Séchilienne, France. Canadian Geotechnical Journal. 42(4), 1105-1115.

Nishii, R., Matsuoka, N., Daimaru, H. and Yasuda, M., 2013. Precursors and triggers of an alpine rockslide in Japan: the 2004 partial collapse during a snow-melting period. Landslides, 10(1), 75-82.

Oppikofer, T., Jaboyedoff, M., Pedrazzini, A., Derron, M.H. and Blikra, L.H., 2011. Detailed DEM analysis of a rockslide scar to characterize the basal sliding surface of active rockslides. Journal of Geophysical Research: Earth Surface, 116(F2).

Pánek, T. and Klimeš, J., 2016. Temporal behavior of deep-seated gravitational slope deformations: A review. Earth-Science Reviews, 156, 14-38.

Pánek, T., Brázdil, R., Klimeš, J., Smolková, V., Hradecký, J. and Zahradníček, P., 2011a. Rainfall-induced landslide event of May 2010 in the eastern part of the Czech Republic. Landslides, 8(4), 507-516.

Pánek, T., Hradecký, J., Minár, J., Hungr, O. and Dušek, R., 2009. Late Holocene catastrophic slope collapse affected by deep-seated gravitational deformation in flysch: Ropice Mountain, Czech Republic. Geomorphology, 103(3), 414-429.

Pánek, T., Šilhán, K., Tábořík, P., Hradecký, J., Smolková, V., Lenart, J., Brázdil, R., Kašičková, L. and Pazdur, A., 2011c. Catastrophic slope failure and its origins: Case of the May 2010 Girová Mountain long-runout rockslide (Czech Republic). Geomorphology, 130(3-4), 352-364.

Pánek, T., Tábořík, P., Klimeš, J., Komárková, V., Hradecký, J. and Šťastný, M., 2011b. Deep-seated gravitational slope deformations in the highest parts of the Czech Flysch Carpathians: Evolutionary model based on kinematic analysis, electrical imaging and trenching. Geomorphology, 129(1-2), 92-112.

Phillips, M., Haberkorn, A., Draebing, D., Krautblatter, M., Rhyner, H., Kenner, R., 2016. Seasonally intermittent water flow through deep fractures in an Alpine rock ridge: Gemsstock, central Swiss Alps. Cold Regions Science and Technology, 125, 117-127.

Price, N.J. and Cosgrove, J.W., 1990. Analysis of geological structures. Cambridge University Press.

Ridl, R., Bell, D. and Villeneuve, M., 2017, April. Application of Finite Element Method of Numerical Modelling to Understand Toe Buckling Deformation in the Southern Alps of New Zealand. In EGU General Assembly Conference Abstracts (Vol. 19, p. 13689).

Riva, F., Agliardi, F., Amitrano, D. and Crosta, G.B., 2018. Damage-Based Time-Dependent Modeling of Paraglacial to Postglacial Progressive Failure of Large Rock Slopes. *Journal of Geophysical Research: Earth Surface*, *123*(1), pp.124-141.

Rocscience 2017. RocData version 5.009, Rocscience Inc. Toronto, Canada.

Rocscience 2019. RS2 2D Geotechnical Finite Element Analysis, version 2019 10.008. Rocscience Inc. Toronto, Canada.

Sandmeier, K.J., 2012. REFLEXW Version 7.0 Manual. Karlsruhe.

Sturzenegger, M. and Stead, D., 2012. The Palliser Rockslide, Canadian Rocky Mountains: characterization and modeling of a stepped failure surface. Geomorphology, 138(1), 145-161.

Tannant, D.D., Giordan, D. and Morgenroth, J., 2017. Characterization and analysis of a translational rockslide on a stepped-planar slip surface. Engineering Geology, 220, 144-151.

Winkler, S., 2018. Investigating Holocene mountain glaciations: a plea for the supremacy of glacial geomorphology when reconstructing glacier chronologies. Erdkunde, 72, 215-234.